*Communications of the Geological Survey of Namibia, **30** (2026), 1-31*

Analysis of sulfide remobilization in boudinaged quartz veins of the K1 prospect and Navachab Gold Mine main pit, Karibib area, central Namibia: implications for gold distribution

Junias K. Ndeunjema[a*], Collen-Issia Uahengo[a*], Josia Shilunga[a], Leonard Mbango[b] & Pamwenatse Vaino[b]

[a]*Department of Geology, University of Namibia*
[b]*Department of Geology, QKR Navachab Gold Mine*

**Corresponding author(s): <cuahengo@unam.na>;<juniaskondja74@gmail.com>*

Abstract :- Orogenic gold deposits are typically characterized by structurally controlled hydrothermal veins that host auriferous sulfide. Remobilization of gold during post-ore metamorphism and deformation plays a critical role in ore localization. This study investigates boudinaged quartz veins (BQVs) at the K1 prospect within the Usakos Dome, central Namibia, which shares geological characteristics with the nearby Navachab deposit in the Karibib Dome.

Detailed field mapping, petrographic observations under reflected light, and gold assays were undertaken to evaluate the influence of structural controls on sulfide remobilization and gold distribution. Petrography reveals ore textures indicative of sulfide remobilization, including `durchbewegung´ structures, chalcopyrite–pyrrhotite intergrowths, and pyrite replacement by pyrrhotite. At Navachab, boudinaged quartz veins are mineralized with sulfides, predominantly pyrite, chalcopyrite, pyrrhotite, as well as minor arsenopyrite, galena, sphalerite, and covellite. Gold assays from Navachab indicate elevated concentrations in boudin necks relative to the boudin bodies, suggesting that well-developed boudinage promotes localized gold enrichment through rheological contrasts between the vein and wall rock. However, this relationship is not clearly established at the K1 prospect.

Field mapping and structural analysis at the K1 prospect indicate that veins earlier thought of as boudinaged, actually represent `apparent´ boudinage, implying that the remobilization process differs from previous interpretations or may not have occurred at all. Although vein density at Navachab exceeds that at K1, it appears to exert limited control on sulfide remobilization and gold grade within individual veins. Instead, structural deformation and vein rheology play a more dominant role in controlling gold redistribution in orogenic vein-type deposits.

Keywords: Remobilization, Sulfides, Boudinaged quartz veins, Spes Bona Member, Oberwasser Member, Okawayo Member, Durchbewegung, Apparent boudinage

Introduction

Orogenic gold deposits are the most significant epigenetic gold systems in metamorphic terrains and account for roughly 70–75% of the world's primary lode gold (Goldfarb *et al*., 2005; Goldfarb & Groves, 2015). These deposits form predominantly from metamorphic fluids generated by converging plates and are associated with accretionary or collisional orogenic zones (Groves *et al*., 1998; Kerrich *et al*., 2000; Gaboury, 2019). Structurally, mineralization occurs in hydrothermal vein systems hosted in brittle to brittle-ductile deformation zones along ancient faults or folds (Groves *et al*., 1998; Goldfarb *et al*., 2001; Kisters, 2005; De Carvalho, 2019; Goldfarb *et al*., 2019). These veins commonly contain sulfide minerals such as pyrite, pyrrhotite and arsenopyrite, which are closely associated with gold (Goldfarb & Groves, 2015).

An important mechanism affecting orogenic gold deposits is metamorphic remobilization by which pre-existing mineralization is redistributed and chemically modified during metamorphism (Vokes, 1969; Marshall & Gilligan, 1987, 1993). It involves the movement of ore-forming elements through solid-state, hydrothermal, or combined mechanisms, leading to the reconcentration and alteration of metals and minerals, particularly during prograde metamorphism and fluid-rock interaction (Cox, 1987; Rutter, 1993; Li *et al*., 2022). Mechanical remobilization requires rheological diver-

gence between sulfides and their host rocks (Marshall & Gilligan, 1987). Gold remobilization in orogenic gold deposits can be achieved through alteration and deformation of structures containing sulfides (Biagioni *et al*., 2020; Hastie *et al*., 2020; Li *et al*., 2023). Brittle-ductile boudinage structures are prime examples of features that record deformation, that form when layers, bodies, or foliation planes with contrasting rheology are stretched and segmented during bulk extension (Goscombe *et al*., 2004; Rodrigues & Pamplona, 2018; Bamberg *et al*., 2022).

Structures that superficially resemble boudinage may in fact be `apparent´ boudinage, which can lead to misinterpretation. Bons & Druguet (2007) note that these features may arise from shear bands, faults, or the opening of fracture jogs. In apparent boudins, beads are joined by thin connecting seams with minimal internal deformation, whereas true boudins exhibit strongly sheared material within the connecting zones (Bons *et al*., 2004).

Previous studies focused on ore remobilization due to metamorphism and deformation in general (Barnes, 1987; Plimer, 1987; Marshall & Gilligan, 1987, 1993; Marshall & Mancini, 1994; Xu & Zhou, 2001; De Roo & Staal, 2003; Houghton *et al*., 2004; Zhao *et al*., 2021; Li *et al*., 2022). Although many orogenic gold deposits display boudinaged quartz veins as evidence of deformation, there is comparatively limited research specifically investigating remobilization processes within these boudinaged vein structures (Amponsah *et al*., 2015; Williams & Blenkinsop, 2024). Understanding these processes is critical, because they directly influence gold concentration, vein geometry, and ultimately exploration strategies in structurally complex terrains.

This study focused on the QKR Navachab Gold Mine and K1 prospect located in the southern Central Zone (sCZ) of the Pan-African Damara Belt, central Namibia (mineral exploration licence EPL 999, Karibib District, Erongo Region). Gold mineralization at the Navachab pit is characterized by semi-massive sulfide lenses and quartz sulfide veins (Kisters, 2005; Wulff *et al*., 2010, 2017; Creus, 2011; Vollgger *et al*., 2015). Previous studies (e.g. Kisters, 2005; Kitt, 2008; Wulff *et al*., 2017) indicated that vein sets oriented at high angles to the bedding and favorably to the stress field are more mineralized than others oriented at low angles. Sheeted quartz veins are irregularly shaped in marble units, with highly varying thicknesses showing pronounced pinch- and swell and boudinage-type structures.

The complex polymetallic ore assemblage in the quartz-sulfide veins and semi-massive sulfide lenses is mostly composed of chalcopyrite, pyrrhotite, arsenopyrite, pyrite, and sphalerite (Dziggel *et al*., 2009). Alteration associated with mineralization led to the quartz-sericite assemblage.

The primary aim of this study is to investigate the remobilization of sulfides within boudinage quartz veins at the K1 prospect (Usakos Dome, Karibib area), and to compare these processes with similar occurrences at the Navachab Gold Mine main pit. By analyzing the orientation, density, and geometry of boudinaged veins, it hopes to establish the relationship between sulfides and gold, providing new insights into structural controls on gold distribution in complex metamorphic terrains.

Geological context

Regional geology of the Karibib district

The northeast-trending intracontinental branch of the Damara Orogen formed as a result of the amalgamation of the Gondwana Supercontinent after break-up of Rodinia and represents the collisional suture between the Congo and Kalahari Cratons (Fig. 1A; e.g. Miller, 1983, 2013; Van Zijl & De Beer, 1983; Gray *et al*., 2008; Schmitt *et al*., 2018). The Neoproterozoic (750-600 Ma) Damara Supergroup is a lithologically heterogenous succession (Poli & Oliver, 2001; Longridge *et al*., 2011), which records the entire orogenic history from rifting and associated rift sedimentation and volcanism, through an oceanic spreading stage with marine sedimentation, to convergence and final continental collision (Miller, 1983; Gray *et al*., 2008; Goscombe *et al*., 2017; Schmitt *et al*., 2018).

The study area is located within the southern Central Zone (sCZ) of the Damara Orogen (Fig. 1B; Johnson, 2005; Kitt, 2008; Wulff *et al*., 2017; Kisters *et al*., 2004; Kisters, 2005; Owen, 2011), which is characterized by kilometer-scale, elongated and ovoid-shaped dome structures, ranging from 10 to 40 km in

length and 4 to 18 km in width, with a southwest-northeasterly trend. This study focuses on the Karibib Dome (Navachab main pit) and the Usakos Dome (K1 prospect), which are separated by the Navachab Syncline (Figs 2A, B). These domes are made up of Damara Supergroup metasediments, which are cored by the Abbabis Metamorphic Complex (Kisters *et al*., 2004; Johnson, 2005; Table 1). Both domes preserve an early D_1 fabric, expressed as bedding-parallel foliation (S_1) in the Chuos Formation and Spes Bona Member; D_2 deformation is observed in the Okawayo Member as isoclinal folding (Table 2). The Usakos Dome's southeastern limb is truncated by a massive, northwest-verging thrust known as the Mon Repos Thrust Zone (MRTZ, Figs 2A, 3; Kisters *et al*., 2004).

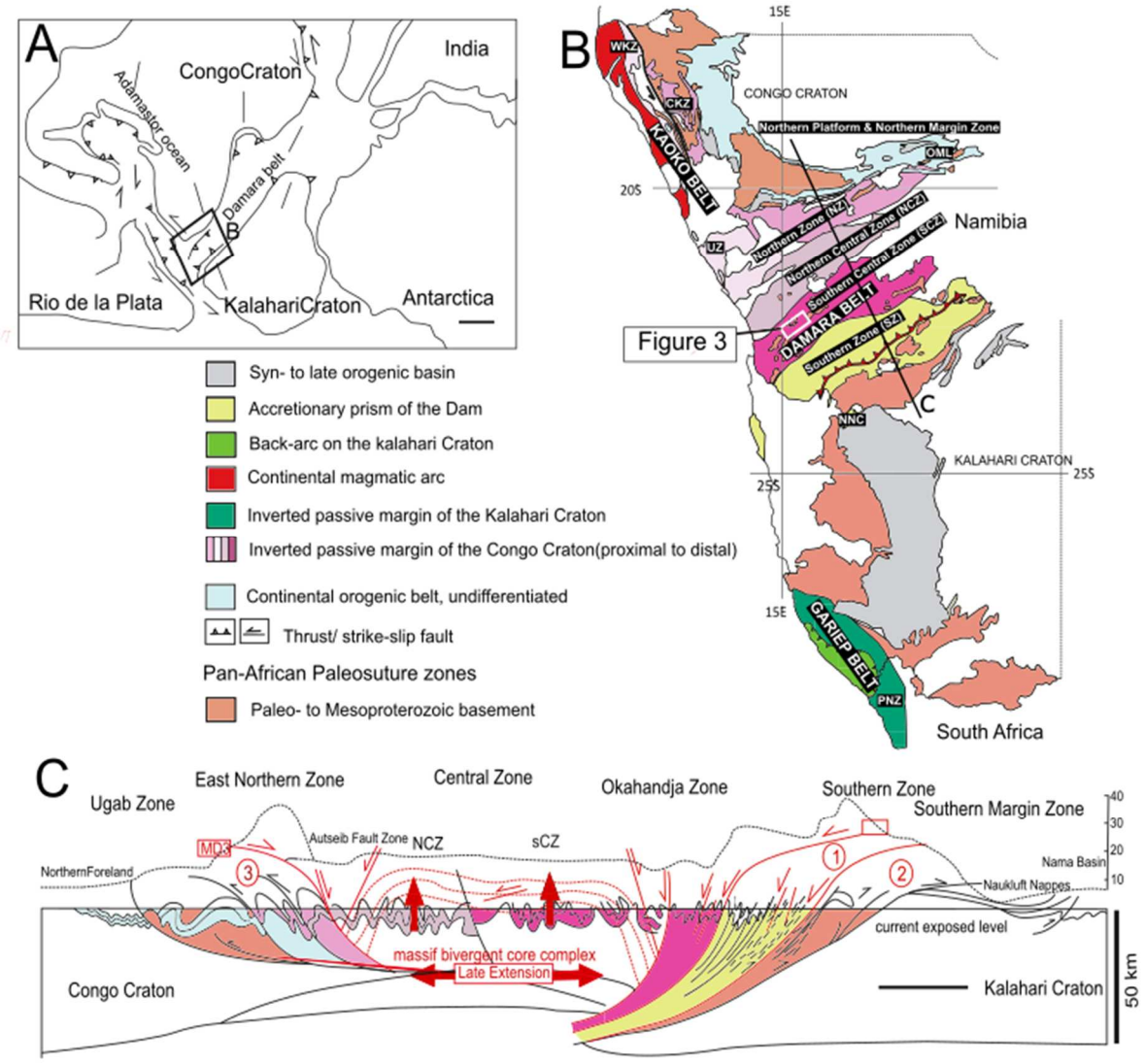

Figure 1. Geology of the study area: (A) collision between the Congo and Kalahari cratons during the Gondwana amalgamation (modified after Longridge *et al*., 2011); (B) tectonostratigraphic zones of Namibia (modified after Miller, 2008), (C) cross-section of the Damara belt illustrating the different tectonostratigraphic zones (modified after Poli & Oliver, 2001).

The Abbabis Metamorphic Complex (AMC) outcrops in an erosional window in the core of the Karibib Dome, southeast of the Navachab open pit, and 3-5 km south of the Usakos Dome (Kisters *et al*., 2004; Kitt, 2008; Steven *et al*., 2014). It is characterized by quartzo-feldspathic, pink to gray gneisses, schists, amphibolite, and pegmatite, which represent the oldest rocks in the area (Miller, 1983; Jacob *et al*., 1978). The Etusis Formation, the

lowest unit of the Damara Supergroup, is exposed along the southeastern limb of the Usakos Dome (Kitt, 2008; Table 1). It consists of thin interbedded meta-arkose, metapelite and metaconglomerate (Miller, 1983; Johnson, 2005; Kitt, 2008), and forms noticeable ridges southeast of the Navachab open pit (Kitt, 2008). The diamictites and dolomitic marker horizons of the Chuos Formation overlie the Etusis Formation (Hoffman *et al*., 1996; Kitt, 2008). Metapelites, composed of well-foliated, dark-gray quartz-biotite+muscovite schists with fine-grained quartzite clasts and porphyroblasts of cordierite (Badenhorst, 1988), are thought to be a small slice of the Chuos Formation. The thick succession of the Kuiseb Formation forms the center of the Kranzberg Syncline, which marks the northwestern and northern extend of the Usakos Dome, and has a normal, shallow-dipping northwestern and a steeply dipping to inverted southeastern limb (Owen, 2011).

Table 1. Stratigraphy of the study area (SG - supergroup, MC – metamorphic complex).

Eon	Supergroup/ Complex	Group	Subgroup	Formation	Member	Lithology
Neoproterozoic	Damara SG	Swakop	Navachab	Kuiseb		Mica schist, minor calc- silcate
				Karibib	Onguati	Mica schist, impure marble, calc-silicate
					Arises River	Massive calcitic marble
					Otjongeama	Impure marble, minor calc-silicate
				Ghaub	Daheim	Amphibolite and metasediments
			Usakos	Arandis	Oberwasser	Mica schist, minor calc-silicate
					Okawayo	Marble, interbedded calc-silicate
					Spes Bona	Mica schist, interbedded calc-silicate
				Chuos		Diamictite, interbedded quartzite and schist
		Nosib		Etusis		Meta-arkose, schist, conglomerate
Meso- to Paleoproterozoic	Abbabis MC					Ortho- and paragneiss, metasedimentary rocks; minor amphibolite

Local Geology

This section summarizes previously documented geological information at the deposit scale, with emphasis on the Navachab and K1 areas.

Navachab main pit

The Navachab pit is located on the steep northwestern limb of the Karibib Dome (Fig. 2A). Although both the Navachab main pit and the K1 prospect occur within the Damara Supergroup (Fig. 3), the stratigraphic units at Navachab display distinct facies characteristics and thickness variations (Kitt, 2008). The open pit exposes a near-complete cross-section through the Swakop Group (Table 1), from the Spes Bona Member in the east to the Oberwasser Member and Karibib Formation in the west. Lithological variations within this succession exert a strong control on quartz veining.

This study focuses on selected areas within the Navachab main pit, i.e. Pushback 3 (PB3) and the Eastern Pit (E1) (Fig. 2B). Work at PB3 was conducted on two levels: (i) Level 69 (L69WPB3) and (ii) Level 74 (L74WPB3) on the western wall (Fig. 2C). The marble-calc-silicate unit (MC), located at the contact between the Okawayo and Spes Bona Members, hosts the high-grade gold mineralization at Navachab.

K1 prospect

The K1 prospect is situated within the hinge of a parasitic fold of the Usakos Dome (Fig. 2A), which prominently exposes the upper stratigraphic units of the Swakop Group (Table 1). At the core of the dome, the Spes Bona Member consists of interbedded calcsilicate felsites, pale-gray metapsammites, and dark-gray to black biotite schists (Fig. 4). Strong folding

and granite intrusions complicate correlations within this unit (Johnson, 2005; Kitt, 2008). The Okawayo Member, exposed along the southwestern limb of the Usakos Dome, is a thin marble unit separating the schistose Spes Bona and Oberwasser Members (Johnson, 2005; Wulff *et al*., 2010, 2017). Its lower part contains intercalated calcsilicate and calcitic marble, while the upper dolomitic section is free of calcsilicate.

The Oberwasser Member comprises a banded siliciclastic succession of dark-gray biotite schists, calcsilicate felsites, and minor carbonate breccia (Badenhorst, 1992; Kitt, 2008). Centimeter-thick tremolite-rich layers provide useful marker horizons within this succession (Johnson, 2005). Overlying this unit, the Karibib Formation contains deformed dolomitic marbles characterized by cream-weathered surfaces and white, sugary fresh textures (Brandt, 1985; Lehtonen *et al*., 1996). Together, these units define the stratigraphy at K1, with the Spes Bona Member at the core, younging through the Okawayo and Oberwasser Members, Karibib and Kuiseb Formations toward the dome margins (Kisters *et al*., 2004; Johnson, 2005; Owen, 2011).

Table 2. Deformation phases in the Navachab area and associated fabrics (after Kisters, 2005).

Deformation	**Fabric**	**Field expression, occurrence and occurrence of fabrics**
Primary	S_0	Primary compositional layering
D1	S_1 and S_0/ S_1	Bedding-subparallel foliation parallel to low-angle shear zones devel-oped in the Chuos Formation and Spes Bona, Okawayo and Oberwasser Members (Arandis Formation); absent in the Etusis and Karibib For-mations; locally developed as transposition fabric (F1 folds; S0/S1 foliation)
Early low-angle shearing		
D2	S_2	Steep- to subvertical (50-80°), NE- to NNE- trending axial planar foliation to F2 folds; variably developed as wide-spaced cleavage (e. g. stylolite in marbles), crenulation or transposition fabric on the NW limb of the Karibib Dome (S0/S2)
Perclinal NW-vergent folding (Karibib Dome) and top-to-the-NW-thrusting (540-550 Ma)	F_2	NE- to NNE-trending, NW-verging, doubly plunging folds, including the first order folds of the Karibib and Usakos Domes and Navachab Syncline
	F_{2a}	Small, uneven parasitic folds (from second order and below), ranging from a few dm to about 10 m in size, double plunging and align with the main F2 folds, which plunge toward the northeast in the open pit.
	F_{2b}	Symmetric folds in quartz veins on the NW limb of the Karibib Dome; similar plunge to F2 and F2b folds, dm- to m-scale; NE-plunging in the open pit
	L_{2a}	Intersection lineation between S2 and S0 or S0/S1 (δ-lineation), shallow northeasterly and south-westerly plunge, parallel to plunge of F2 first-order folds; northeasterly plunge in open pit
	L_{2b}	Weakly-developed, regional mineral stretching lineation (e. g. stretched breccia fragments, lapilli, mineral aggregates); NW-SE trending, parallel to L2a

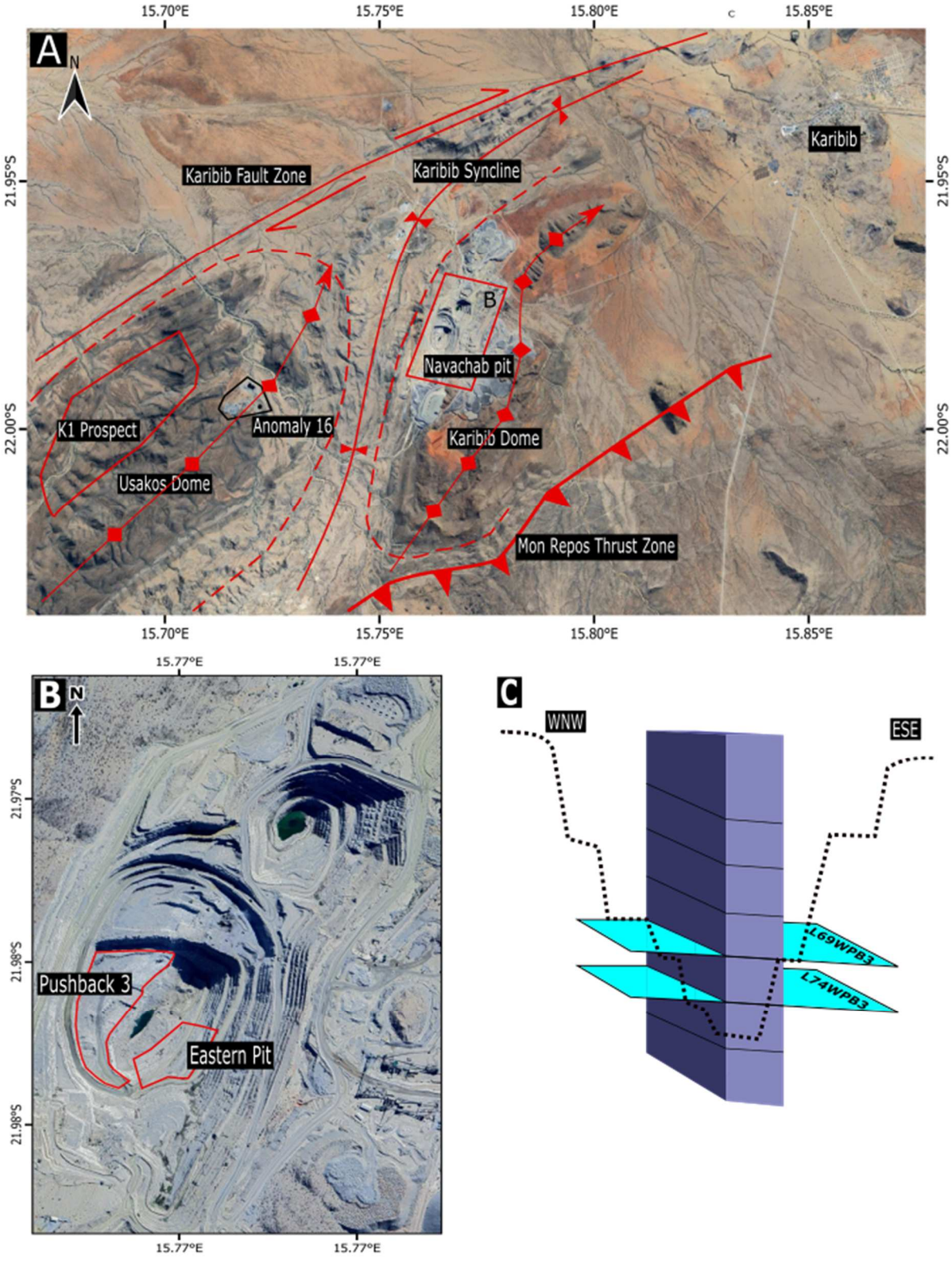

Figure 2. (A) Locality map with red polygons indicating study areas, i.e. Navachab main pit on the western limb of the Karibib Dome marked B, K1 prospect in the nose of a parasitic fold of the Usakos Dome. Also shown are the Mon Repos Thrust Zone, Karibib Thrust Zone and the Navachab Syncline; (B) plain view of the Navachab pit, with red polygons delineating the two areas of interest within the pit: Pushback 3 and Eastern Pit; (C) stereoscopic outline of the Navachab pit in Pushback 3 showing the two levels studied, i.e. level 69 (L69WPB3) and level 74 (L74WPB3) on the western wall of Pushback 3.

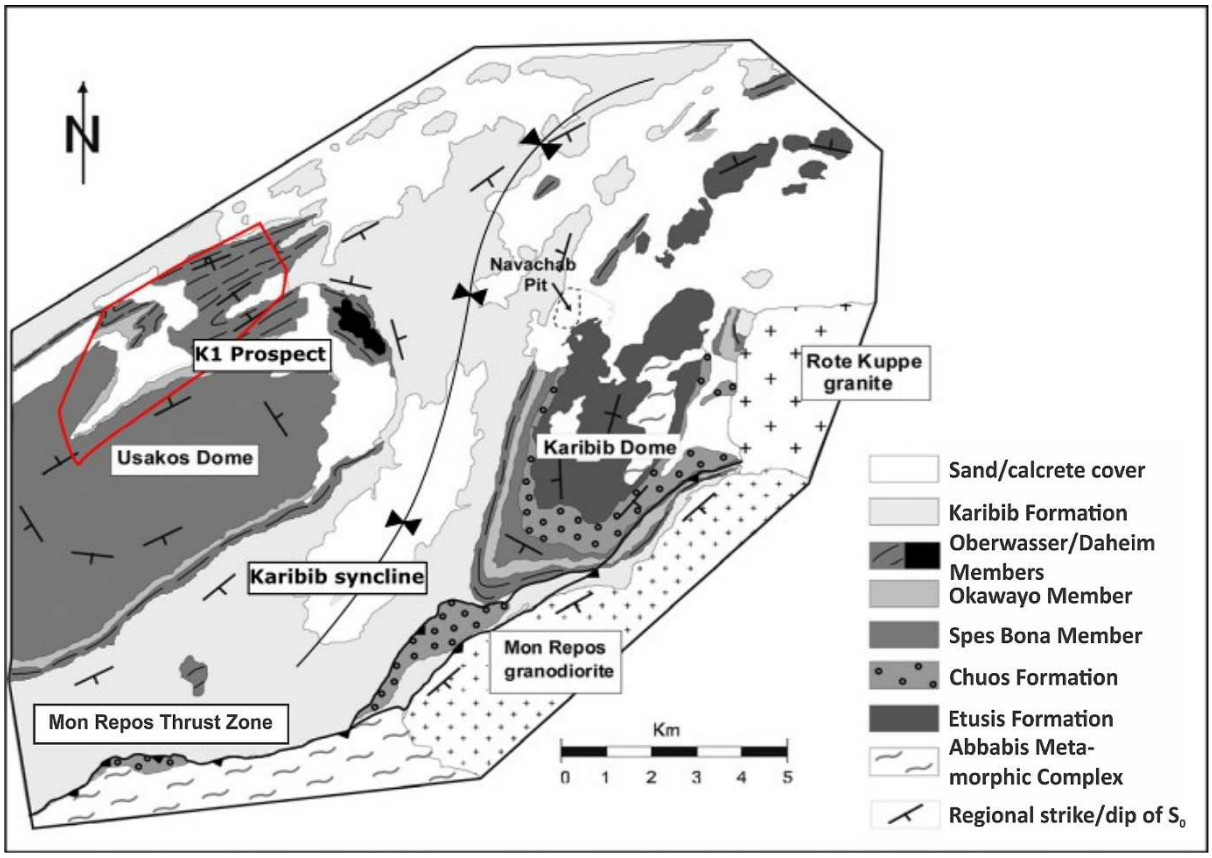

Figure 3. Simplified geological map of the Karibib and Usakos Domes (modified after Kisters *et al.*, 2004); Abbabis basement gneisses and the lower units of the Damara Supergroup are exposed in the core of the Karibib Dome, whereas the Usakos Dome is cored by higher stratigraphic levels, i.e. the Spes Bona Member of the Arandis Formation. The Pan-African-age Mon Repos granodiorite and Rote Kuppe granite intrude the eastern parts of the study area. In the south, Abbabis gneisses have been thrust over stratigraphically much higher marbles of the Karibib Formation along the Mon Repos Thrust Zone.

Methodology

Sampling

Boudinaged quartz veins were sampled at Pushback 3 on levels 69 (L69WPB3) and 74 (L74WPB3), in the Eastern Pit and at the K1 prospect in the Usakos Dome. A total of 30 samples was collected, comprising 15 from Pushback 3, seven from the Eastern Pit, and eight from the K1 prospect. The study aims to explain remobilization in the boudinaged quartz veins by comparing gold grades and petrographic features in the boudin body and neck of the same vein. For each BQV, four samples were collected, where possible. Two samples were obtained from the boudin body domain, while the remaining two samples were taken from the neck (Fig. 4). Of the two samples taken from each domain, one sample was used for geochemical gold assay, and the other for petrographic studies in polished section. Not all BQVs were large enough to yield four samples that would provide representative results. Where possible, the vein was divided into four samples in the field. However, in most cases, the entire vein was collected and cut into sections at the camp to obtain representative samples, which were placed into individual sample bags.

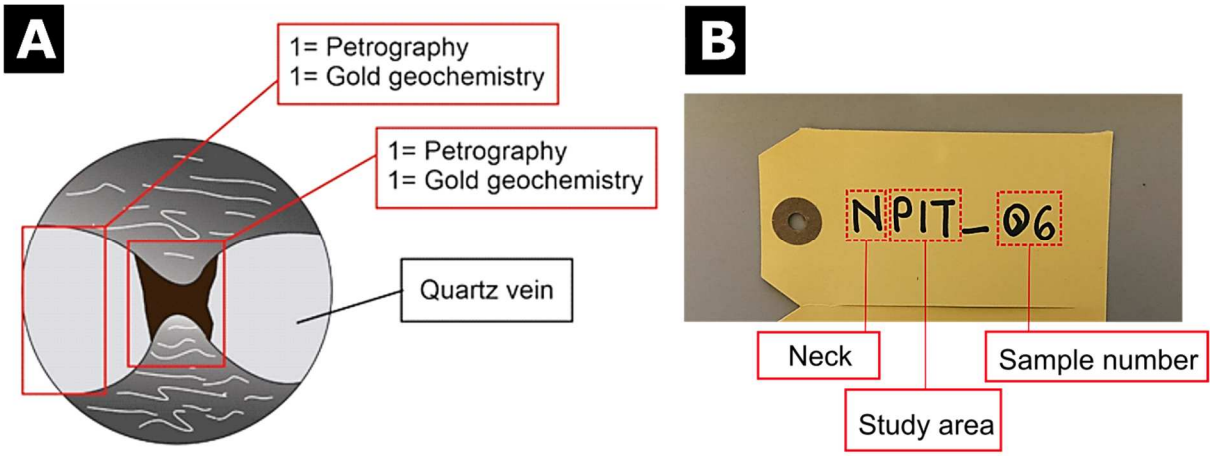

Figure 4. (A) Sampling strategy of the boudinaged quartz veins (BQV) for petrographical and geochemical analysis at Navachab and K1; (B) naming of samples by boudinage position, study area and sample number.

Geochemical gold assay

Gold grade was determined by melting and separation from other metals using the fire assay procedure, commonly referred to as cupellation, at the QKR Navachab Gold Mine lab. The procedure includes:

Sample Preparation Process Flow: The milling process aims to obtain a finer particle size, ensure homogeneity, and achieve effective gold liberation. After drying the samples for eight hours, they are weighed, labelled, and placed in a labelled box. The mill is cleaned with quartz pebbles between samples to prevent contamination. Particle size distribution is determined on the first sample using a 75µm sieve. The dried sample is then weighed and used to calculate the percentage of mass of material passed through the sieve, which should be between 93% and 95%. If not in the range, the milling is repeated until the desired range is achieved.

Balance Room: The main aim of fluxing is to extract/concentrate gold from its ore. For fluxing, 30 g of the sample was weighed, and 30 g of the right flux added and mixed with the sample. The mixture was poured into a crucible. Copper sulphate was added to acts as a marker to differentiate specific batches and to aid in the later stages of separating precious metals (gold/silver) from the copper-rich lead button. In addition, 5 ml of silver nitrate was added to further the collection of gold (making the prill).

Fusion: Crucibles were put in a fusion furnace for 90 minutes at 1100˚C. After changing into liquid state, the mixture is poured into a mold. Gold and other metals segregate at the bottom (lead button), while the slag (containing flux, calcium fluoride, etc.) floats at the top.

Hammering: After cooling and solidifying the lead button is hammered to separate it from the slag, and placed in a tray to be weighed.

Cupellation: Cupels first were warmed for a few minutes to the same temperature as in the cupellation furnace. Lead buttons were placed in the cupels and stayed in the cupellation furnace for an hour. The cupels are composed of bone ash, which absorbs lead and base metals during the process. As a result, only silver and gold prills remain. The prills were allowed to cool for approximately 20 minutes before undergoing the prill dissolution process.

Prill Dissolution: Prills were placed into a 10 ml volumetric flask, to which nitric acid was added to break them. HCl was added to dissolve gold, and lanthanum chloride to settle any base metals. After cooling, distilled water was added and the flask was covered and shaken to homogenize the solution.

AAS Analysis: The solution was analysed by atomic absorption spectroscopy (AAS), calibrated by using Navachab lab standards.

Assay graph plots

Assay data from boudin necks and bodies were analyzed using a combination of exploratory, comparative, and estimation-based statistical visualizations. Overall assay trends and data overlap were first assessed using linear scatter plots including all samples. Differences in central tendency and data dispersion between

domains were evaluated using box plots; only veins sampled both in the neck and boudin body domains were plotted for an informed comparison. Agreement and systematic bias between neck and boudin body assays were examined using difference-versus-average (Bland–Altman) plots incorporating Welch's t-test statistics (Altman & Bland, 1983; Welch, 1947) to account for unequal variances. Finally, estimation plots were employed to quantify differences between group means, with effect sizes and 95% confidence intervals reported.

Petrography

Petrographic analyses of the boudinaged quartz veins (BVQs) were conducted using a reflected light microscope at the laboratories of Namibia's Ministry of Mines, Industries and Energy. Imaging was performed under 4x/0.13 magnification. The rock samples were prepared as polished sections, which were examined in at least two different areas of each section. This approach was intended to ensure the identification and characterization of the representative distribution and textural features of sulfides within the sample. Detailed imaging and interpretation aimed at a comprehensive understanding of the sulfide mineralogy and texture within the polished sections.

Results

Navachab pits: Pushback 3 (PB3)

Field relations

Pushback 3 of the main pit exposes the Okawayo and Oberwasser Members, from east to west. However, the present study only covered the Oberwasser Member at level 69 western wall (L69WPB3) and level 74 western wall (L74WPB3), due to accessibility in the pit and the presence of well-exposed boudinaged quartz veins for sampling purposes. Figure 5 shows a schematic diagram of boudin neck and body dimensions, as measured in the field. The Oberwasser Member is dominated by biotite schist and biotite schist-calcsilicate. The biotite schist predominantly consists of fine-grained biotite, feldspar and quartz, while the biotite schist-calcsilicate is made up of fine-grained feldspars with minor quartz and biotite. The strata dip steeply (70˚ to 80˚) WNW, striking NNE-SSW.

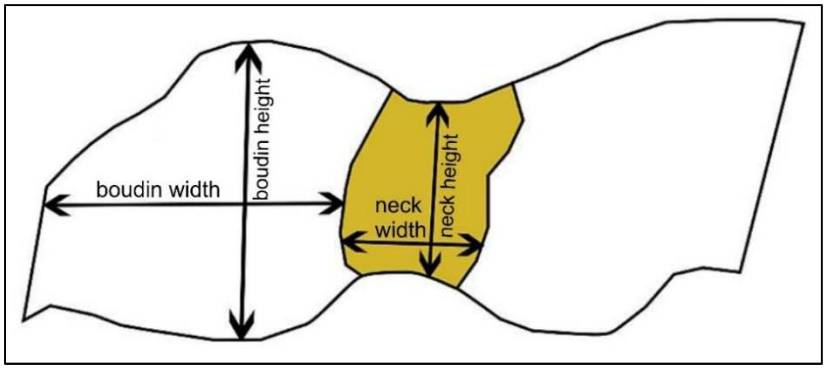

Figure 5. Schematic drawing illustrating width and height of boudin body and neck, respectively.

The main visible quartz veins consist of milky white to gray smoky quartz. The boudins are mainly dominated by milky quartz, while the boudin necks consist of smoky quartz (Fig. 6A). The strike of the BQVs is on average 30˚, with a dip of approximately 60˚ NW. The BQVs occur in most cases close to one another, spaced ± 2 m apart (Fig. 6). The geometry is not constant in all BQVs. Boudins are only partially separated, as they remain linked by a boudin neck that is variably filled with sulfides, ranging from partial to complete infilling (Fig. 6). Bboudin necks are about 2 to 3 cm thick, while the boudins have a width of ± 12 cm and a thickness of ± 5 cm.

The main sulfides in the BQVs are pyrite, pyrrhotite, chalcopyrite, with minor bornite (Fig. 7). Pyrrhotite was observed to occur massively in the boudin necks, while other sulfides like pyrite, chalcopyrite and bornite only occur as fine grains or fracture infills (Fig. 6). According to Aghaei *et al*. (2023) a milky white coloration signifies little or no mineralization, although previous studies at Navachab (Dziggel

et al., 2009; Wulff *et al*., 2010, 2017) have found through photomicrographs and geochemical analyses that there are fine grains of gold in milky white quartz, indicating that variable gold concentrations are associated with specific quartz varieties. Sulfides in the boudins appear to be more widely spaced, while sulfides at the rims/edges of the boudins spread into the wall rock (Fig. 6).

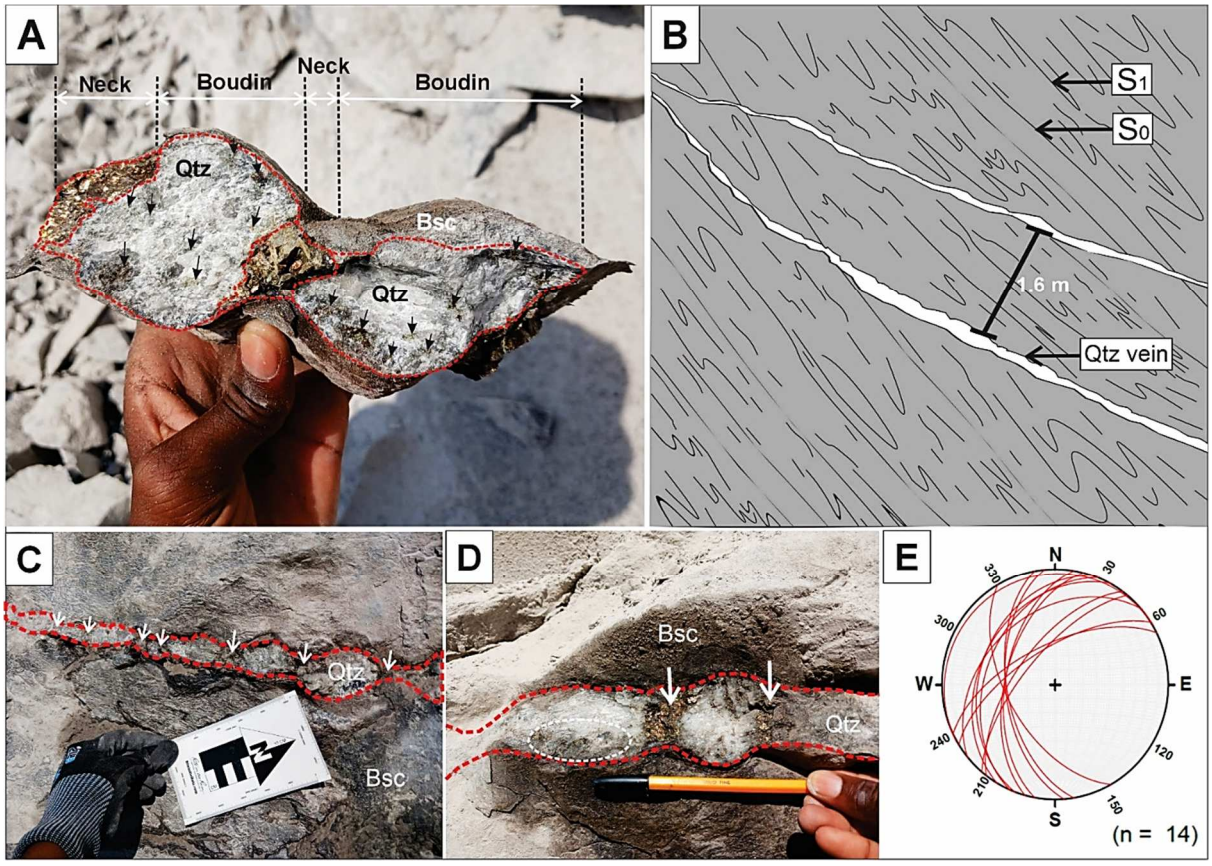

Figure 6. Summary of observations in Pushback 3: (A) BQV with sulfide filled boudin neck and some small disseminated sulfide grains indicated by black arrows within the boudin; (B) schematic diagram of the distribution of BQVs and relation with bedding (S_0) and foliation (S_1); (C) BQV (Qtz) in biotite schist - calcsilicate (Bsc), with arrows indicating sulfides in the boudin neck; (D) massive sulfides in Bsc of the boudin necks (white arrows) - the white dotted circle in the boudin body shows more widely space sulfide grains; (E) stereographic plot in lower hemisphere for 14 BQVs averaging a trend of 030˚ and dip of 45˚ NW.

Geochemical assays

Assay results from boudin and neck domains show fluctuating gold concentrations, with the highest grade found in the neck (26.6 ppm) and the lowest in the boudin domain (0.03 ppm; Fig. 8A). In general, boudins have a lower average grade than neck samples; however, there are individual boudin samples with higher grades than found in the necks of other BQVs (Fig. 8A). Box plot analysis shows that neck samples exhibit a higher median grade relative to the boudin samples, accompanied by a narrow interquartile range, which is low but relatively higher than for the boudin, reflecting slightly fluctuating assay values with limited dispersion below 20% of the data (Fig. 8B). Linear regression of the Bland–Altman difference-versus-average data yields a slope of 1.067 with a y-intercept of 5.637 and an x-intercept of −5.725 (Fig. 8C). The slope is close to unity, and the reciprocal slope (1/slope = 0.9375) is also near unity, indicating only minor proportional bias between neck and boudin assay values. Estimation plots further quantify this difference, showing a mean difference of 0.6525 ppm, with most data points falling within the 95% limits of agreement, also supporting consistency between the two data sets.

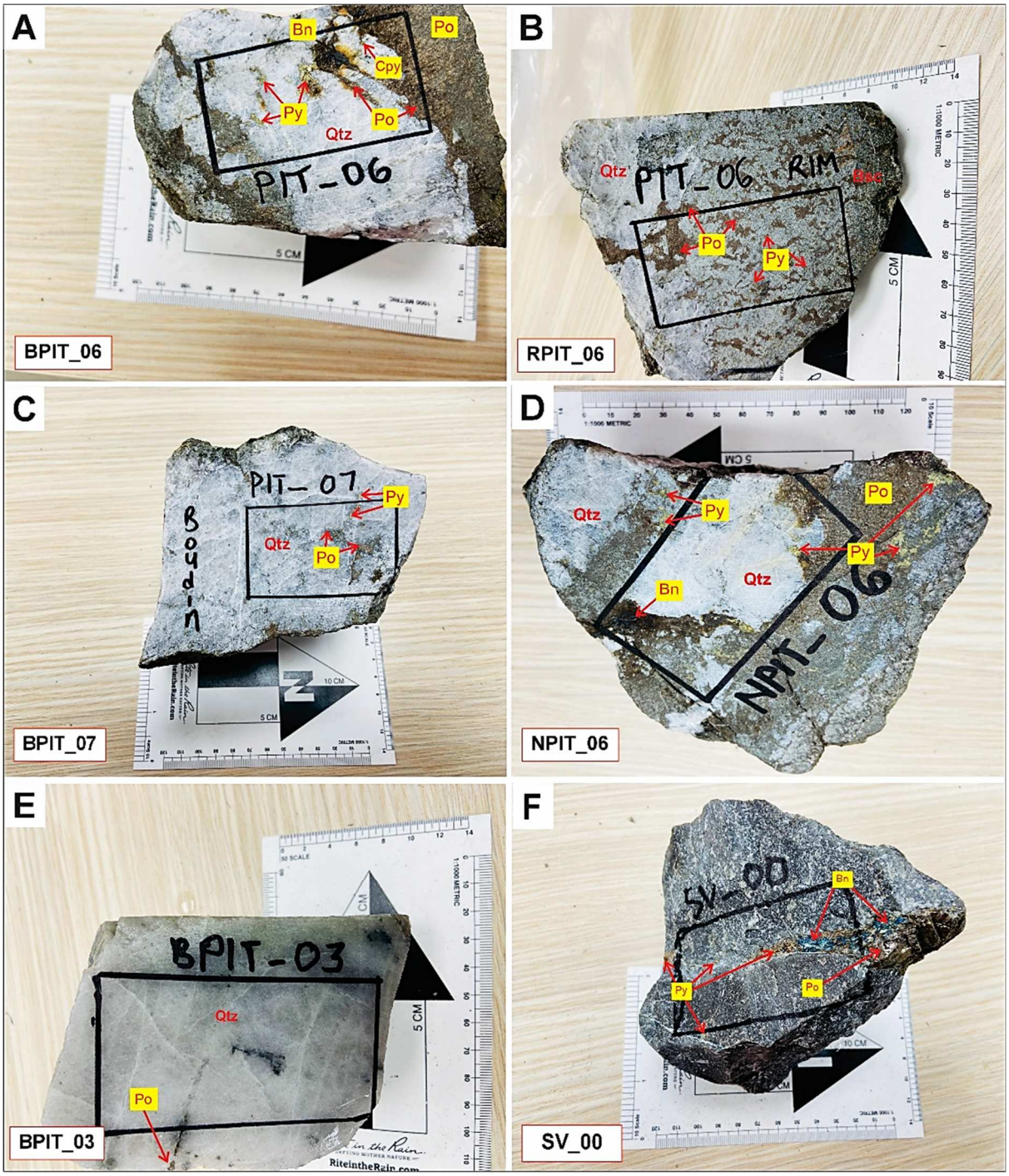

Figure 7. Summary of observations in Pushback 3 (Navachab main pit): (A) sample taken from a boudin indicating sulfides such as pyrite grains (Py), massive pyrrhotite (Po), disseminated chalcopyrite (Cpy) and minor bornite (Bn); (B) BQV sample taken from the margin between vein (Qtz) and host rock (Bsc), showing significant sulfide disseminations of pyrrhotite (Po) and pyrite (Py); (C) boudin sample of a BQV with minor disseminated pyrite (Py) and pyrrhotite (Po); (D) boudin neck sample of a BQV, dominated by massive pyrrhotite (Po), but also containing minor pyrite (Py) and bornite (Bn); (E) pyrrhotite (Po) grains in boudin sample of milky white BQV; (F) fracture filling of bornite (Bn), pyrrhotite (Po) and pyrite (Py).

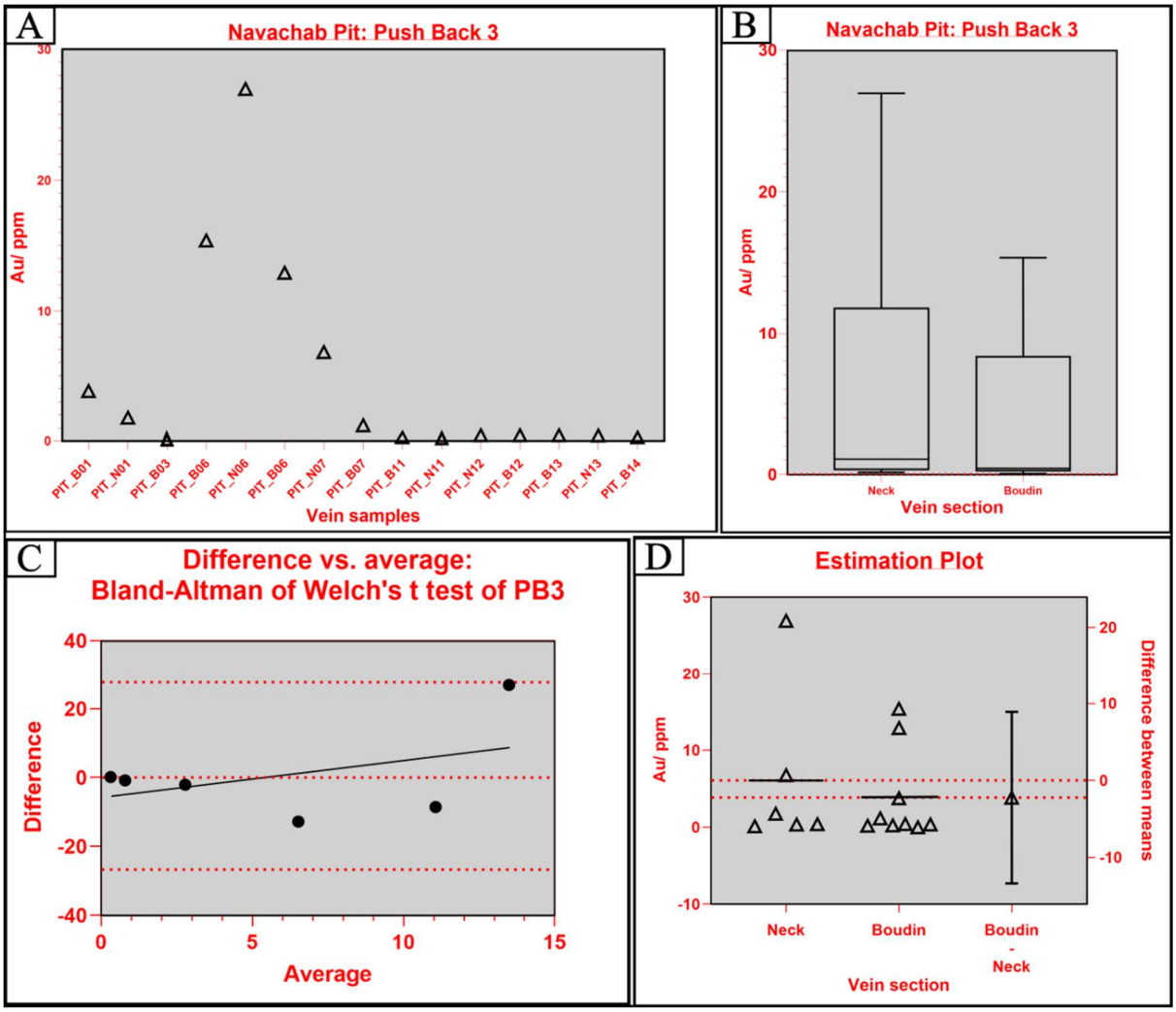

Figure 8. (A) Linear scatter plot of assay results from vein neck and boudin domains showing overall data distribution and trend; (B) box plot comparison of neck and boudin assays illustrating differences in median and interquartile range; (C) Bland–Altman difference-versus-average plot assessing agreement between neck and boudin assays, also indicating the mean difference and 95% limits of agreement; (D) estimation plot showing the difference between mean assay values for neck and boudin domains with associated 95% confidence intervals.

Petrography

The primary sulfides identified are pyrite, pyrrhotite, chalcopyrite, and subordinate amounts of arsenopyrite. These minerals are predominantly found as crack infill within covellite, sphalerite, and galena in the boudin bodies, but also occur in massive form within the boudin necks of the BVQs. The replacement dynamics between the sulfides in this assemblage are a defining characteristic. Chalcopyrite is known to replace pyrite and pyrrhotite, whereas pyrrhotite replaces pyrite and chalcopyrite (Fig. 9; see also Qian *et al*., 2011; Zhang *et al*., 2020). In the boudin, the rim replacement of pyrrhotite by chalcopyrite is significant, suggesting a slow transformation at the mineral surfaces. This delayed shift at the contact zones between pyrrhotite and pyrite (Fig. 9B) and between chalcopyrite and pyrrhotite (Figs 9A & G) is a sign of slow deformation processes (Qian *et al*., 2011; Helpa, 2015).

In the matrix of pyrrhotite, rounded, tiny pyrite inclusions are observed locally in boudin neck samples (Fig. 9K), producing a `durchbewegung´ texture, which is suggestive of deformation and remobilization (Marshall & Gilligan, 1987; Zhao *et al*., 2021). In support of this, chalcopyrite also partially appears as micro-inclusions in pyrrhotite and pyrite. Minor disseminated chalcopyrite and pyrite exhibit plastic deformation, resulting in rounded or elongated grains (Fig. 9D) under high-temperature conditions, where minerals are deformed without fracturing (Rincon, 2022). Pyrrhotite exhibits a spot-like texture (Figs 9J & K), which is caused by brecciation due to deformation.

Minor arsenopyrite forms micro-inclusions in pyrite, which is especially evident in boudin neck samples (Figs 9D & L). Pyrite, chalcopyrite, and pyrrhotite occur as inclusions within boudins, while covellite is primarily found in massive form. Covellite inclusions are observed in the pyrrhotite matrix of boudin necks, which have suffered more substantial deformation and are distinguished by spot-like textures (Fig. 9K). Massive sphalerite engulfs other sulfides as crack infill. Brecciation and brittle fracturing of sphalerite probably is the result of late-stage deformation, presumably after the peak of ductile deformation and metamorphism.

Navachab pits: Eastern Pit (E1)

Field relations

The Eastern Pit (E1) is located east of Pushback 3, and it exposes most, if not all of the Spes Bona Member (lower schist). Lithologically like the Oberwasser Member (upper schist), the Spes Bona Member is dominated by fine-grained biotite schist, quartz-biotite schist and calcsilicate. The biotite schist is well foliated, but appears massive and consists mainly of biotite, plagioclase and K-feldspar, with minor quartz; abundant garnet occurs in the schists and at the contact with quartz veins (Figs 6 & 10). Like the Oberwasser Member, the strata are striking NNE-SSW and dipping at approximately 75˚ SE.

BQVs strike 53˚ NE and are slightly shallower dipping than the BQVs in the Oberwasser Member (32˚ SE; Fig. 10). Quartz appears milky white in some areas and reddish orange in others due to oxidation. Distribution of BQVs in the wall rock is not constant, but on average veins are spaced at 2.5 m intervals. Boudin neck and swell structures are not clear in some BQVs, but domino boudins are evident. The boudins have an average thickness between 3 and 3.5 cm. Sulfides are not readily visible in the field due to high oxidation, and have a dark purple to black color. Sulfides are massively distributed in the boudin necks of the BQVs (Fig. 10).

Geochemical assays

Assay results from boudin and neck domains show that the neck samples have higher Au-grades than the boudin body samples, with the highest grade being 11.35 ppm (neck) and the lowest 0.34 ppm (boudin body domain; Fig. 11A). The difference in Au-grades between the quartz vein samples is not constant. Box plot analysis shows that boudin samples have a higher median grade than neck samples due to an unequal number of samples analyzed from each domain, with a narrow interquartile range (Fig. 11B). Linear regression of the Bland–Altman difference-versus-average data yields a slope of 2.828, with a y-intercept of -5.520 and an x-intercept of 1.952 (Fig. 11C). The slope is close to unity, and the reciprocal slope (1/slope = 0.3536) indicates a proportional bias between the two methods, with differences increasing at higher averages, suggesting underestimation at low values, and agreement at an average around 1.952. Although the mean of the boudin group was higher than that of the neck group, the difference was not statistically significant (Welch's t-test, $t = 1.811$, $df = 1.03$, $P = 0.315$), and the small sample sizes and unequal variances ($F = 30.17$, $P = 0.024$) limit the reliability of this comparison (Fig. 11D).

Petrography

Pyrrhotite characteristically forms tiny grains scattered throughout the matrix and fracture infills. The occurrence of chalcopyrite often indicates a late-stage alteration or replacement process (Fig. 12). Tiny chalcopyrite inclusions in pyrrhotite point to a dynamic mineral environment during formation, and suggest a major textural link, where pyrrhotite may have largely replaced chalcopyrite (e.g. Fig. 12D). Chalcopyrite is mainly replaced by pyrrhotite. Minor inclusions of arsenopyrite highlight the potential for gold mineralization as arsenopyrite is often associated with auriferous deposits. A massive matrix of covellite might indicate that it has formed through alteration of chalcopyrite (Tagirov *et al*., 2016). `Durchbewegung´ textures are present where rounded clasts of pyrite are carried and transported in a matrix of sphalerite and covellite (Figs 12E, F, H & I). Quartz is the dominant gangue mineral, coexisting with deformed sulfides. Brecciation and brittle fractures in sphalerite, which are probably the result of late-stage deformation (presumably after the peak of ductile deformation and metamorphism) are infilled with pyrite being replaced by pyrrhotite (Figs 12H & I).

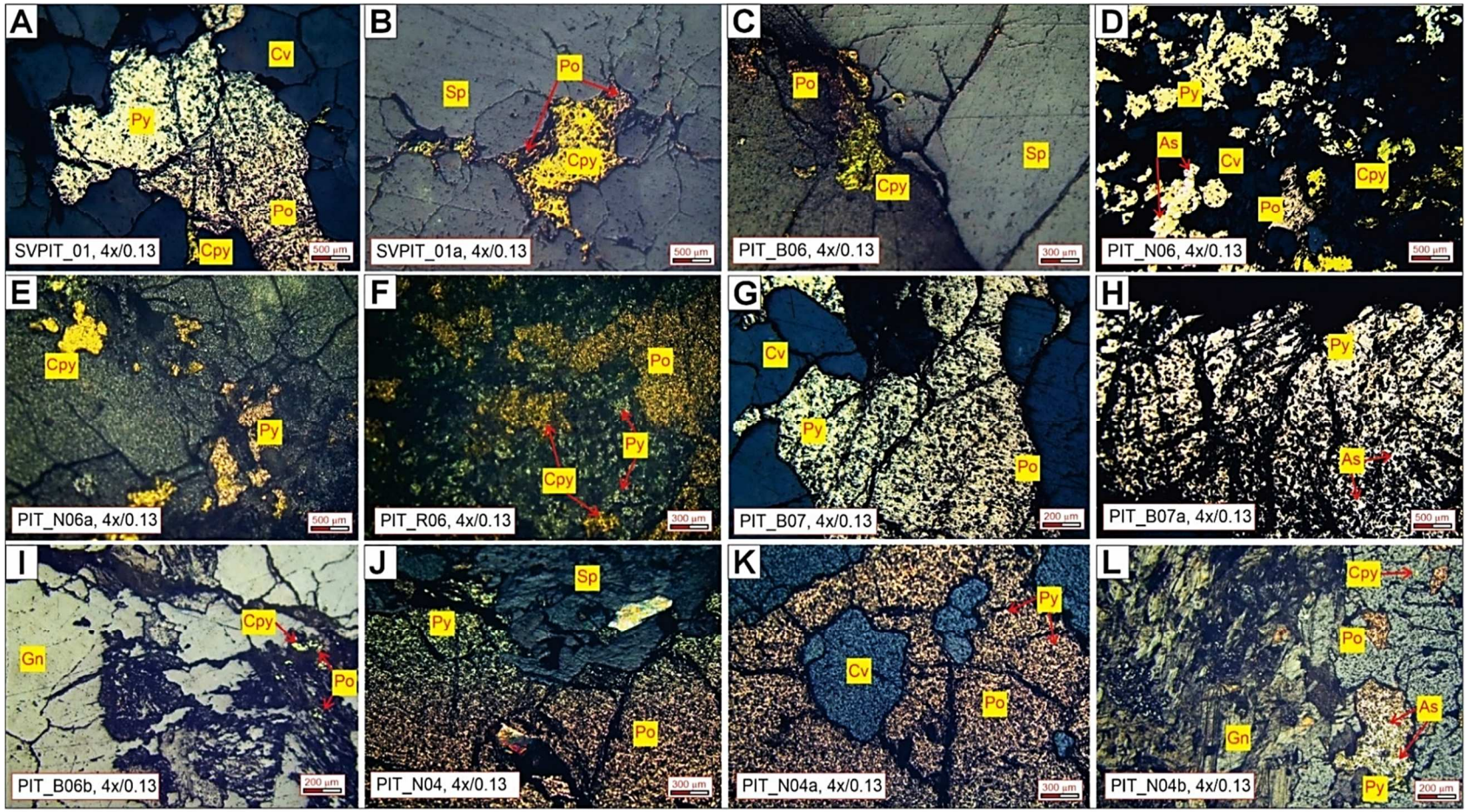

Figure 9. Representative photomicrographs of ore minerals in BQVs under reflected light microscopy (main pit, Pushback 3): (A) massive matrix of covellite with crack infilling of pyrite being replaced by pyrrhotite and chalcopyrite in the boudin; (B & C) massive sphalerite matrix containing pyrrhotite at the rims of chalcoyrite; (D & E) chalcopyrite inclusions in pyrite, which also contain micro-inclusions of arsenopyrite, and chalcopyrite replacement by pyrrhotite in D; (F) chalcopyrite inclusion in massive pyrrhotite matrix, and pyrite forming stains in the matrix of the BQV rims at the wall rock contact; (G) gradual pyrite replacement by pyrrhotite producing a spot-like texture within a covellite matrix; (H) massive, highly fractured pyrite with micro-inclusions of arsenopyrite; (I) massive galena with disseminated individual chalcopyrite and pyrrhotite grains; (J) pyrite replacement by pyrrhotite in sphalerite matrix; (K) covellite inclusions in massive pyrrhotite matrix; (L) brecciated galena matrix hosting pyrrhotite, small chalcopyrite grains and pyrite with arsenopyrite inclusions.

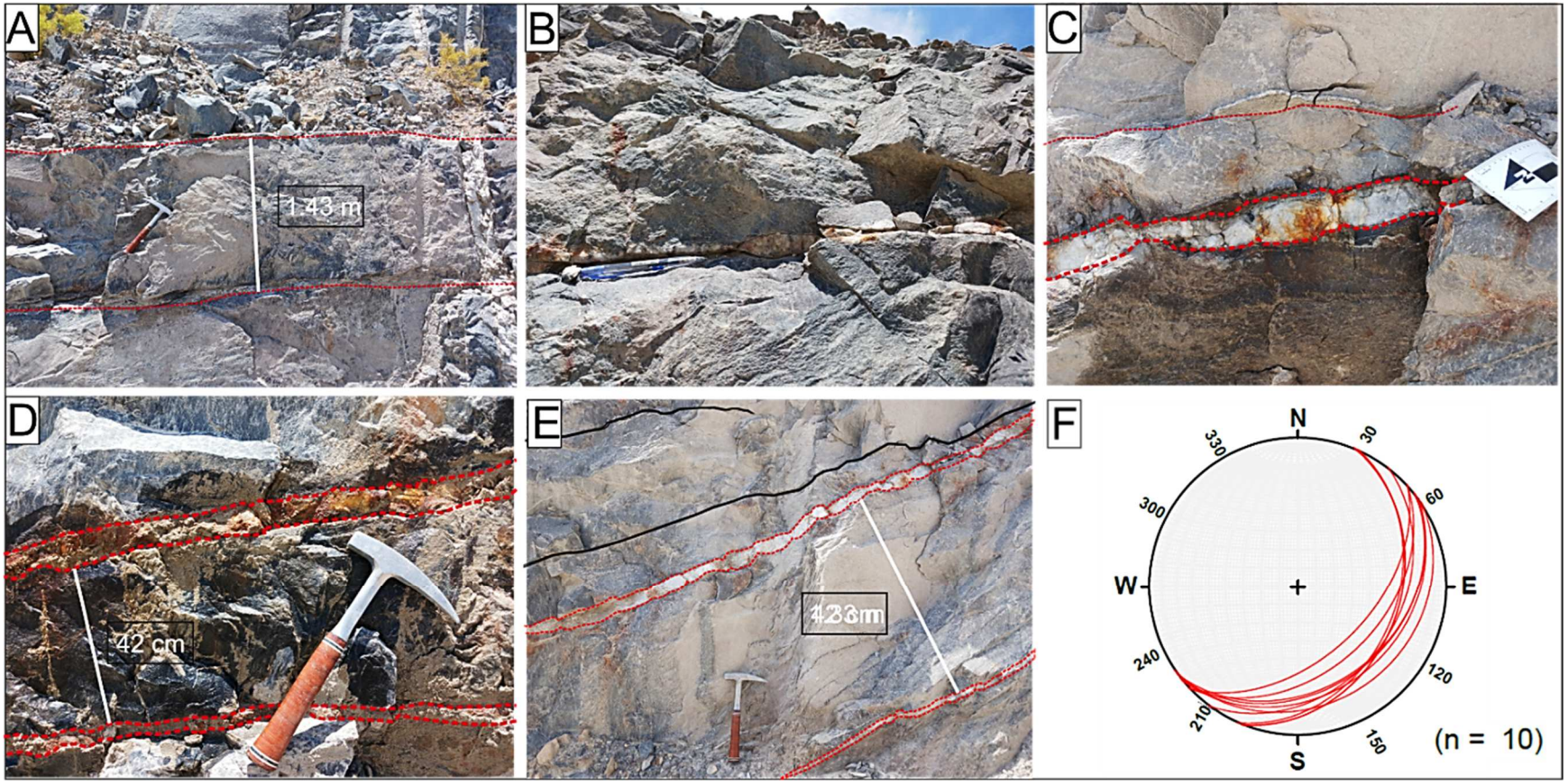

Figure 10. Summary of observations in the E1 pit: (A) Two sub-horizontal BQVs some 1.43 m apart and about 6 cm thick; (B & C) BQV parallel to bedding with minor sulfides in the necks; (D) two BQVs spaced about 42 cm apart, with thickness of 5 cm (top) and 3 cm (bottom); (E) quartz vein with distinct boudinage structure containing garnets at the contact with the biotite schist-calcsilicate host rock signifying alteration; (F) lower hemisphere stereographic net representing structural measurments of ten BQVs in the E1 pit, striking 53˚ (NE) and dipping at an average angle of 32˚ SE.

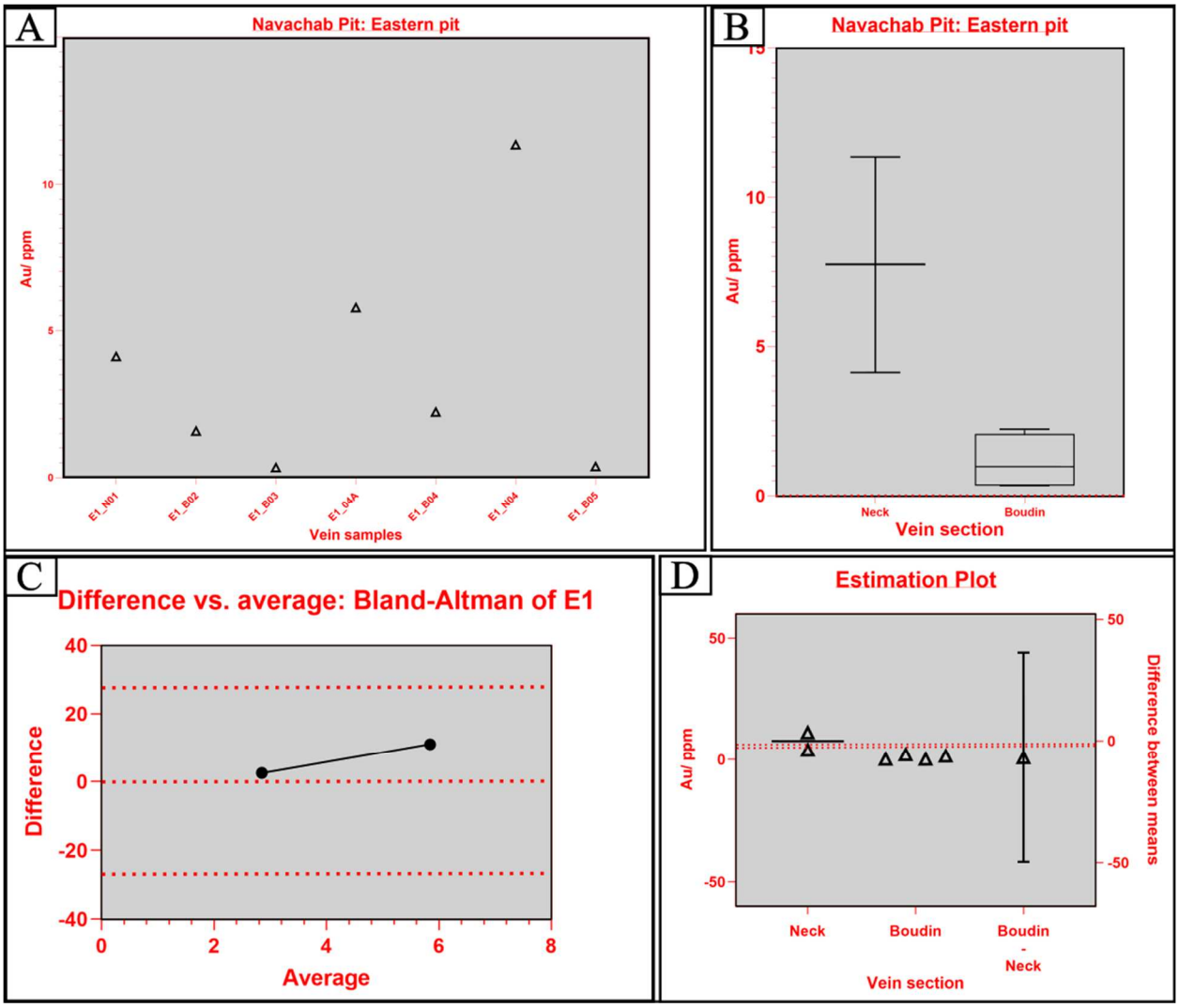

Figure 11. (A) Linear scatter plot of assay results from vein neck and boudin domains showing overall data distribution and trend; (B) box plot comparison of neck and boudin assays illustrating differences in median and interquartile range; (C) Bland–Altman difference-versus-average plot assessing agreement between neck and boudin assays, also indicating the mean difference and 95% limits of agreement; (D) estimation plot showing the difference between mean assay values for neck and boudin domains.

K1 Prospect

Field relations

Mapping and vein distribution

The K1 prospect is characterized by a major Z-fold, with minor parasitic M-folds in the fold hinge (Fig. 13). Stratigraphically, the Spes Bona Member is overlain by the Okawayo Member, consisting of the marble - dolomitic marble (MDM) and marble - calcsilicate (MC) units, which in turn are succeeded by the Oberwasser Member schist. The amphibolites of the Daheim Member (Ghaub Formation) are located at the contact of the Oberwasser Member with the dolomitic marbles of the overlying Karibib Formation (Table 1). Well-exposed pavements reveal highly folded marble and calcsilicate rocks within the Okawayo Member. Northwest striking quartz veins were mapped mainly at the contact of the upper schist of the Spes Bona Member with the marble – calcsilicate of the Okawayo Member, with vein density increasing toward the fold hinge of the Z fold (Figs 13 & 14). This is due to the difference in competence between the carbonate and siliciclastic units, which causes maximum fracturing during folding. According to Roberts & Stromgard (1972), less competent layers have non-planar cleavage, which reflects variation in the orientation of the local XY-plane (Fig. 15). There is no cleavage at the neutral point (Fig. 15E).

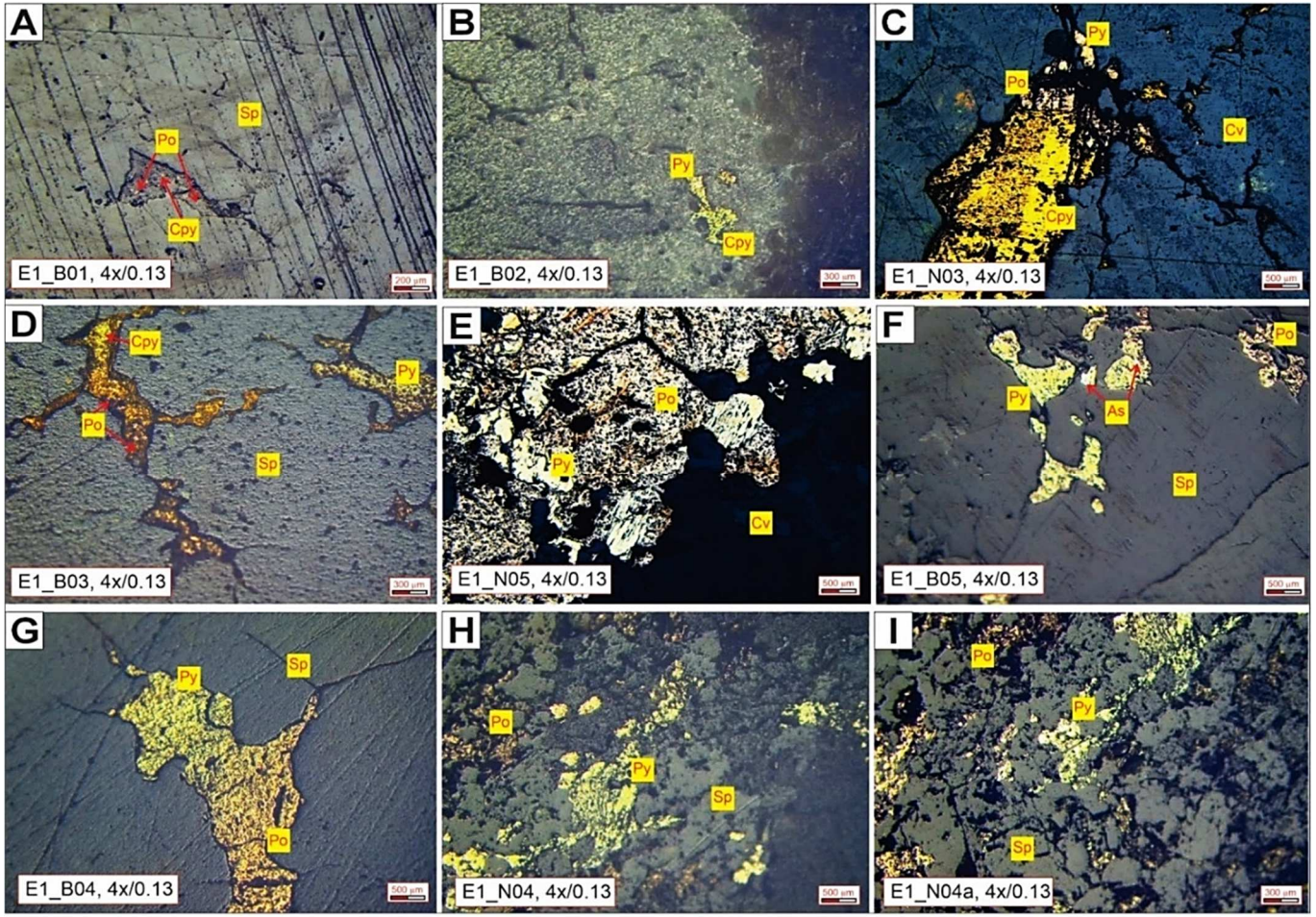

Figure 12. Photomicrographs of BQVs from E1 pit under reflected light: (A) finely disseminated pyrrhotite and chalcopyrite in sphalerite matrix; (B) chalcopyrite replacement by pyrite; (C) fracture infill of massive chalcopyrite being replaced by pyrrhotite, with small inclusions of pyrite; (D) chalcopyrite inclusion in pyrrhotite and pyrite with pyrrhotite rims, all within fractures of sphalerite; (E) covellite brecciation with gangue quartz containing pyrrhotite with pyrite inclusions forming a `durchbewegung´ texture; (F) pyrite fracture filling in sphalerite matrix with arsenopyrite inclusions being replaced by pyrrhotite; (G) pyrrhotite replaced by pyrite in sphalerite matrix; (H & I) brecciated sphalerite containing pyrite as inclusions, with pyrrhotite filling its fractures.

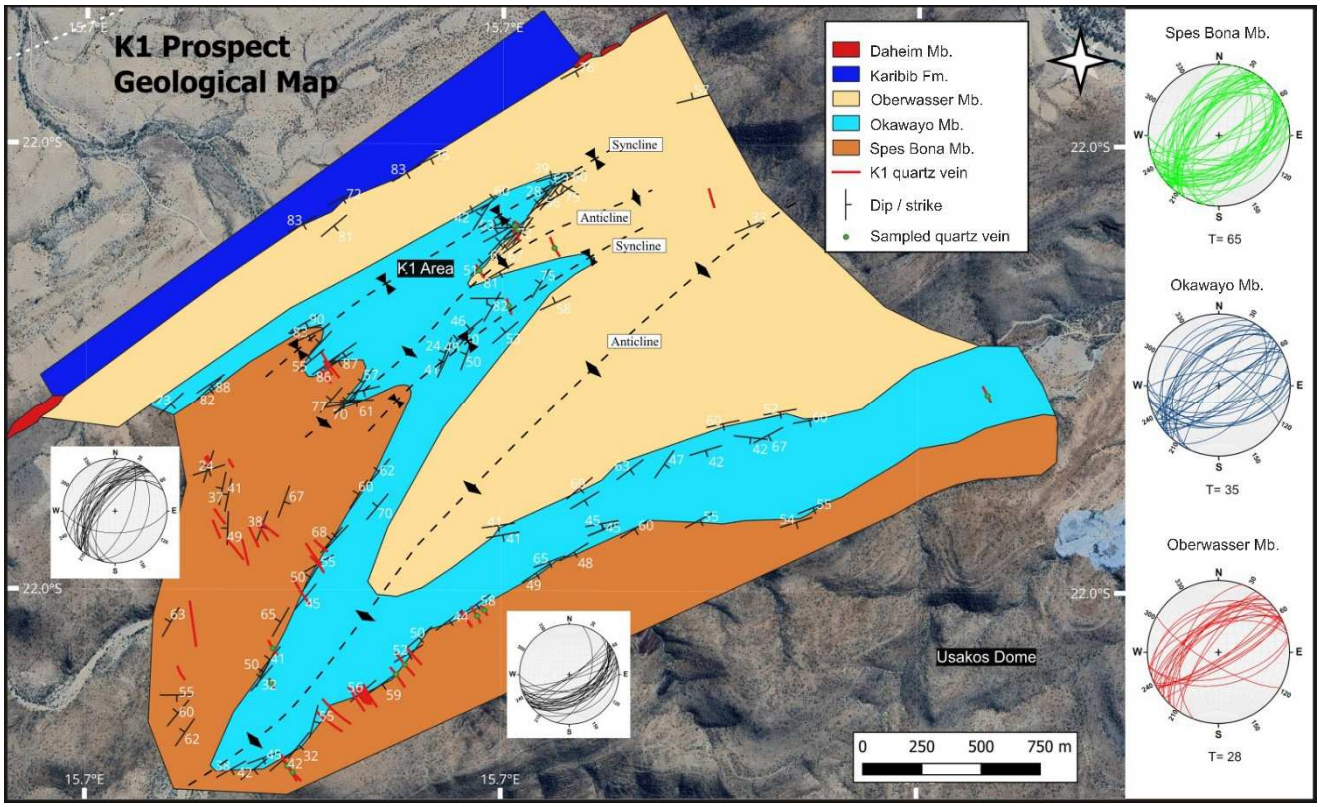

Figure 13. Geological map of the K1 prospect, showing the Z-fold of the Usakos Dome, high vein density toward the fold hinge of the anticlinal fold and delineated approximate anticlinal and synclinal axes; bedding measurements for each unit are represented by stereonet to the right of the image.

Quartz veins

Quartz veins collapse and become inflated during emplacement in marbles, without any vein-parallel stretching. $S_{0/1}$ is deflected around the beads and cuts across the space between the beads (Fig. 14). Mainly N- to NNW–trending (350°–360°) quartz veins display apparent boudinage rather than true boudinage. In high-strain zones within the marble, these apparent boudinaged veins are strongly attenuated and separated (Figs 12B & 14A), reflecting the pronounced rheological contrast between the marble host rock and the quartz vein.

Quartz veins in the siliciclastic units (Spes Bona and Oberwasser Members) do not show any well-defined boudinage structures (Fig. 14B). There is a strong lithological control on the development of the veins, i.e. veins are present in the dolomitic marble, but absent in the calcitic marble. Shear-band boudinaged veins were only identified within the marble. According to Rodrigues & Pamplona (2018) the shear-band boudin shape develops during the final stages of deformation and includes the formation of blunt-tip domains (i.e. rounded or thickened ends of boudins), and furthers secondary shear planes (Goscombe *et al.*, 2004; Fig. 15). There are no visible sulfides within the quartz veins, indicating they are unmineralized (Fig. 14B).

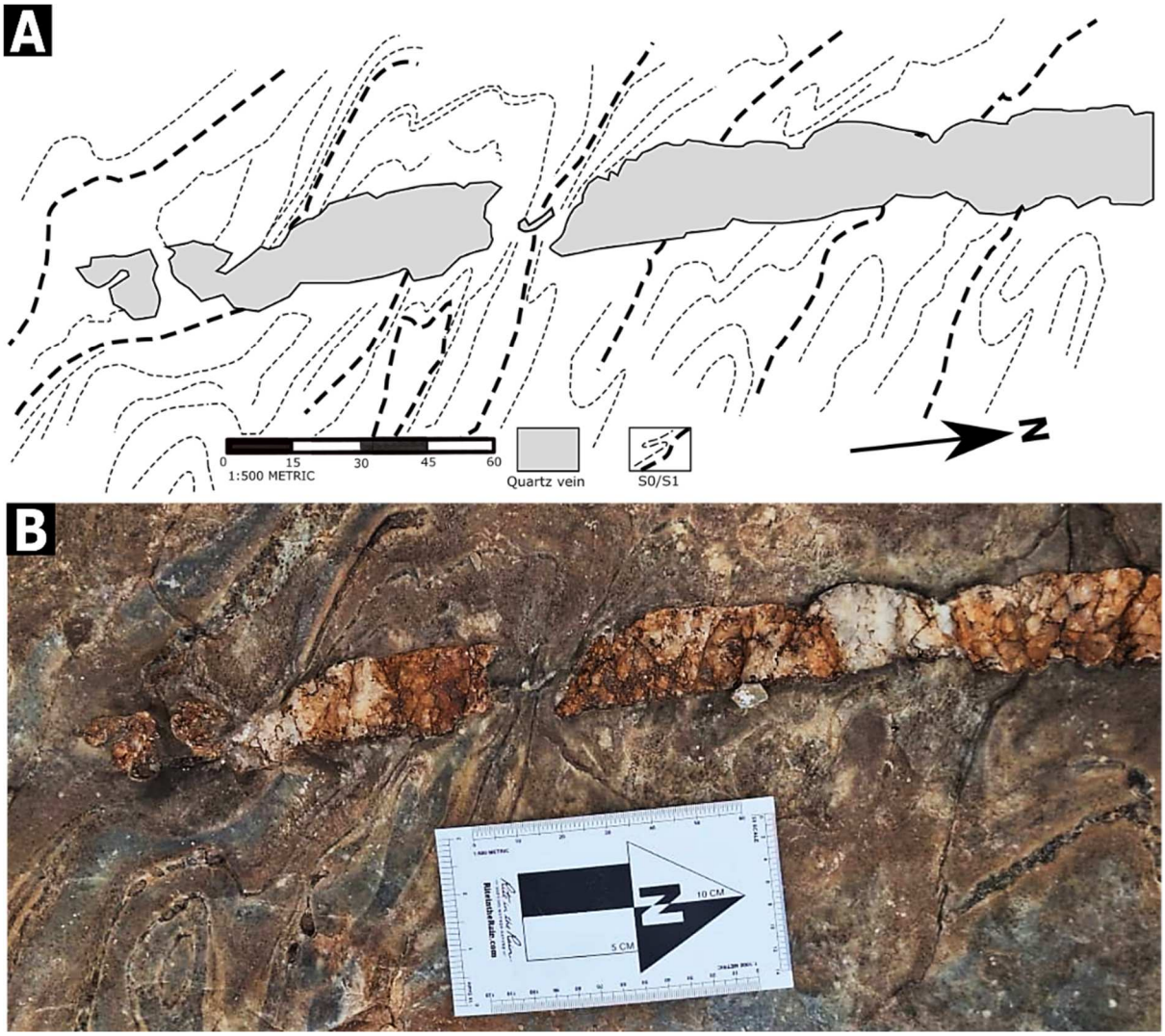

Figure 14. (A) Schematic drawing of a quartz vein that underwent inflation causing $S_{0/1}$ to deflect around the beads and cut across the space between them; (B) N-trending quartz vein in the marble - dolomitic marble unit (MDM)

Geochemical assays

Assay results from boudin bodies and necks generally show higher Au-grades in the boudin body, with the highest grade in the boudin (2.39 ppm) greater than the highest grade in the neck (2.25 ppm); however, the lowest grade was also found in a boudin (0.03 ppm) (Fig. 16A). In sample K1_07 Au-grades are approximately the same in both boudin and neck. Box plot analysis shows that boudin samples have a higher median grade than neck samples, which is due to an unequal number of samples analyzed from each domain, with a narrow interquartile range indicating limited variability and only minor fluctuations in assay values (Fig. 16B). Linear regression of the Bland–Altman difference-versus-average data yields a slope of -1.143 with a y-intercept of 0.2457 and an x-intercept of 0.2150 (Fig. 16C). The slope is close to 1, and the reciprocal slope (−0.8750) shows a nearly proportional inverse bias between the data sets, with little constant offset but increasing divergence at higher values. Estimation statistics (Fig. 16D) show a higher mean grade in boudin samples; however, the wide 95% confidence interval (−8.92 to 9.99) indicates considerable uncertainty, likely reflecting limited and unequal samples.

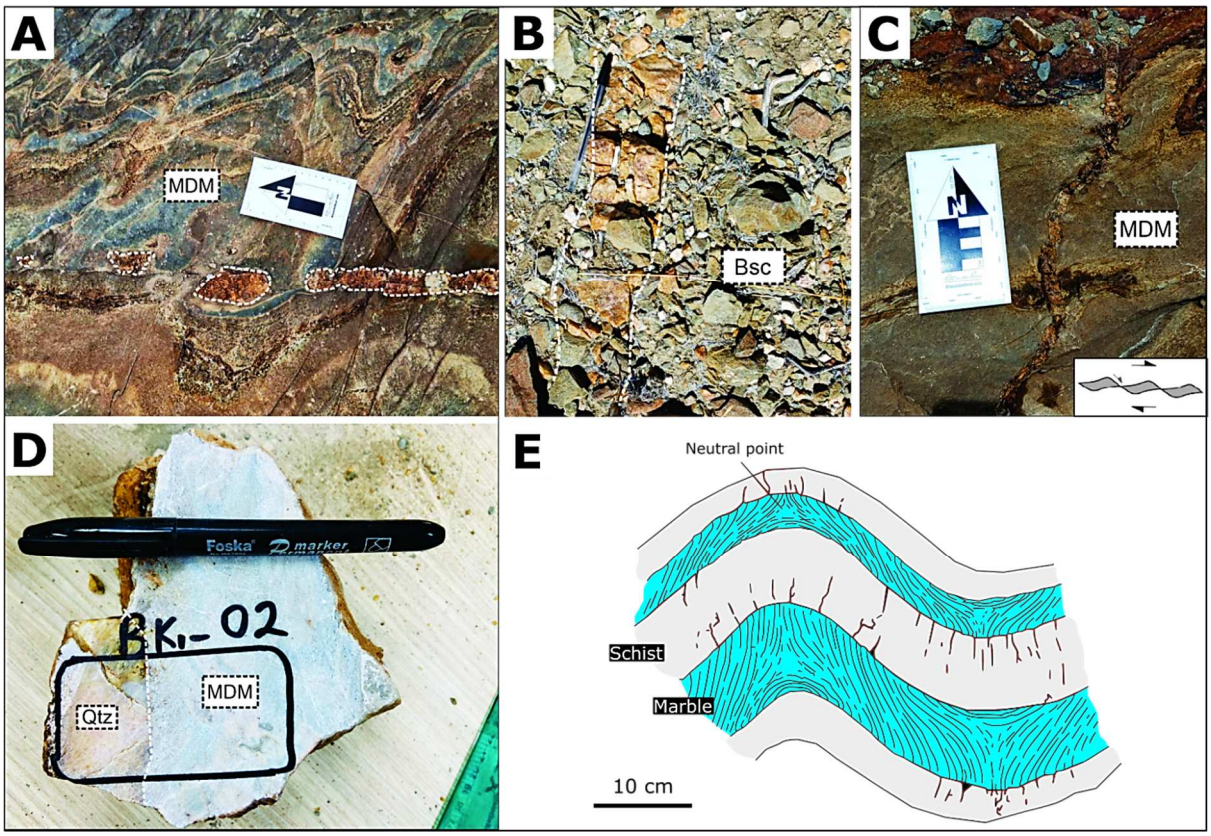

Figure 15. Summary of observations at the K1 prospect: (A) Apparent boudinage of quartz veins in MDM; (B) quartz vein in biotite schist - calcsilicate (Spes Bona Member); (C) shear-band boudinaged quartz vein in MDM and schematic diagram (adapted from Rodrigues & Pamplona, 2018); bottom right of the image); (D) sample BK_02 of a boudinaged quartz vein (Qtz) within MDM; (E) schematic model of high vein density formation during folding of layers with different competence (modified after Robert & Stromgard, 1972), explaining vein distribution at K1.

Petrography

The BQVs at K1 are characterized by small grains of disseminated pyrite, pyrrhotite and minor fine-grained chalcopyrite, which is incorporated in the galena matrix, exhibiting brittle deformation and fracturing (Fig. 17). As observed in other study areas (Pushback 3 and E1 in the Navachab main pit), quartz occurs as small grains within the galena matrix and in fractures, predominantly within the boudin body. Pyrrhotite frequently forms inclusions within pyrite (Fig. 17A). Galena is predominantly observed in BQVs from the marble - dolomitic marble unit (MDM), whereas BQV samples from biotite schist - calcsilicate units (Bsc) mostly contain a sphalerite matrix. Pyrite occurs intergrown with gangue minerals, predominantly quartz, within a massive sphalerite matrix. Additionally, disseminated grains of pyrrhotite and pyrite are present within the galena matrix, indicating complex mineralogical associations and potential multi-stage sulfide formation processes.

Discussion

Microstructural evidence of sulfide remobilization

The main sulfides identified are pyrite, pyrrhotite, chalcopyrite, covellite, sphalerite and galena, with minor arsenopyrite. According to Kitt (2008), Wulff *et al*. (2010) and Dziggel *et al*. (2009), the ore assemblage present in quartz-sulfide veins and semi-massive sulfide lenses is mostly composed of chalcopyrite, pyrrhotite, arsenopyrite, pyrite, and sphalerite. Galena and covellite commonly occur as minor or late-stage sulfides, often forming

intergrowths, rims, or matrix phases associated with primary ore minerals in sulfide systems. However, studies at the Navachab deposit (i.e. Kitt, 2008; Wulff *et al*., 2010) indicate that galena is only present in trace amounts and covellite is not reported among the primary sulfide assemblage.

Sulfides display complex interactions, including `durchbewegung´ and replacement textures, indicating the effects of deformation, which are observed in most areas (e.g. Figs 9K & 10E). `Durchbewegung´ refers to a process involving disruption, separation, kneading, milling, and rotational movement of competent ore minerals within an incompetent sulfide matrix (Barnes *et al*., 2018; Zhao *et al*., 2021; Li *et al*., 2022; Raisch *et al*., 2025). Inclusions of sulfides in the matrix, such as pyrite included in pyrrhotite (Fig. 9J), covellite included in pyrrhotite (Fig. 9K) and arsenopyrite included in pyrite, are evidence of significant internal remobilization, suggesting that the sulfides were subjected to high strain, which allowed for the movement and reconfiguration of sulfide minerals within the matrix (e.g. Rincon *et al*., 2024). Pyrite exhibits an alignment parallel to the tectonic foliation (Fig. 12E), which results from mechanical remobilization during deformation, reflecting the stress conditions prevailing during formation, consistent with Rincon *et al*. (2024).

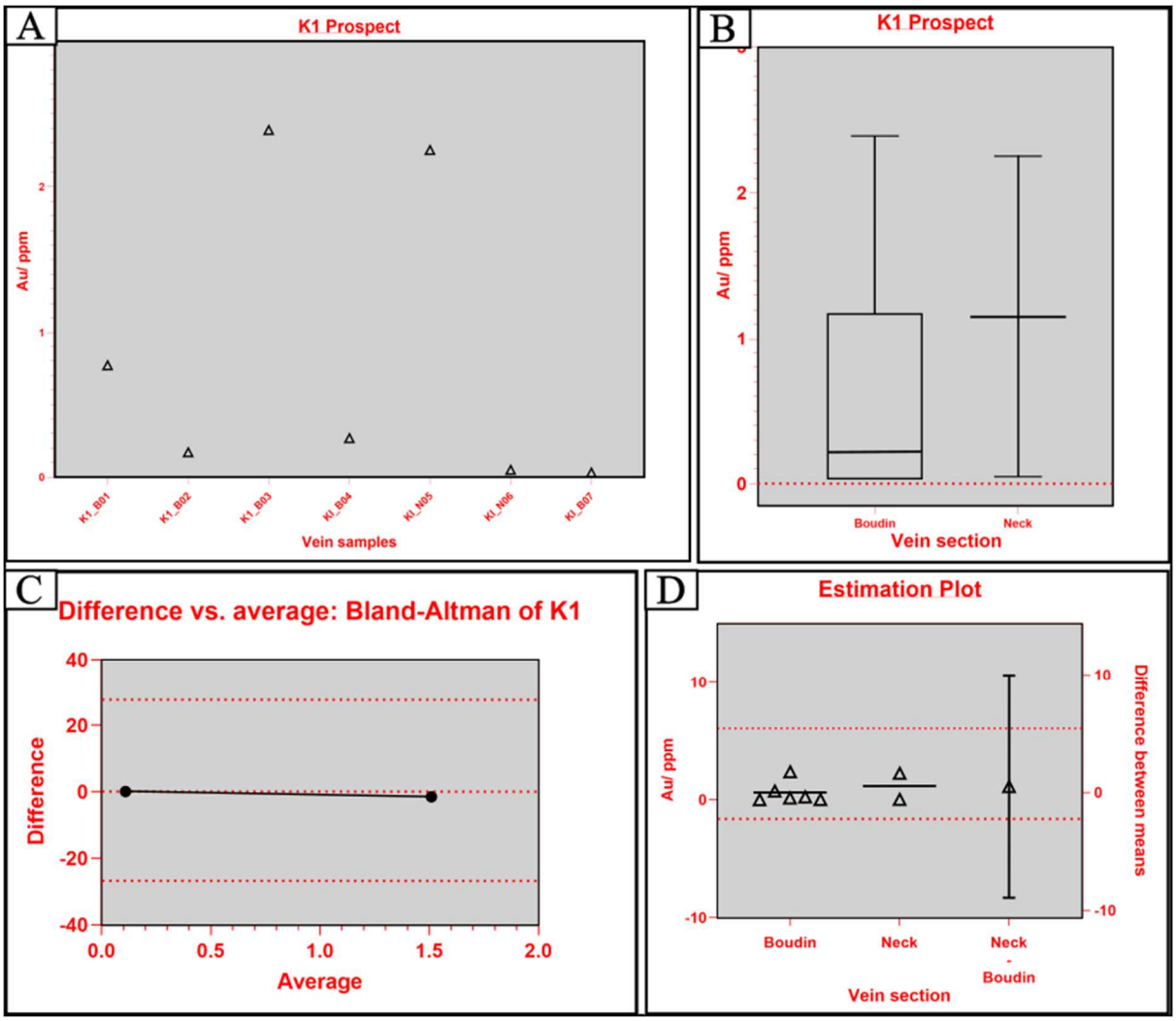

Figure 16. (A) Individual Au-assay values show no clear overall trend, although boudin domains generally exhibit higher grades than necks; (B) box plot analysis indicates a higher median Au-grade in boudin samples with limited variability; (C) Bland–Altman difference-versus-average analysis reveals a near-proportional inverse bias between the data sets with minimal constant offset; (D) estimation statistics show higher mean Au-grades in boudin samples, but wide confidence intervals, indicating substantial uncertainty due to limited and unequal sample sizes.

.

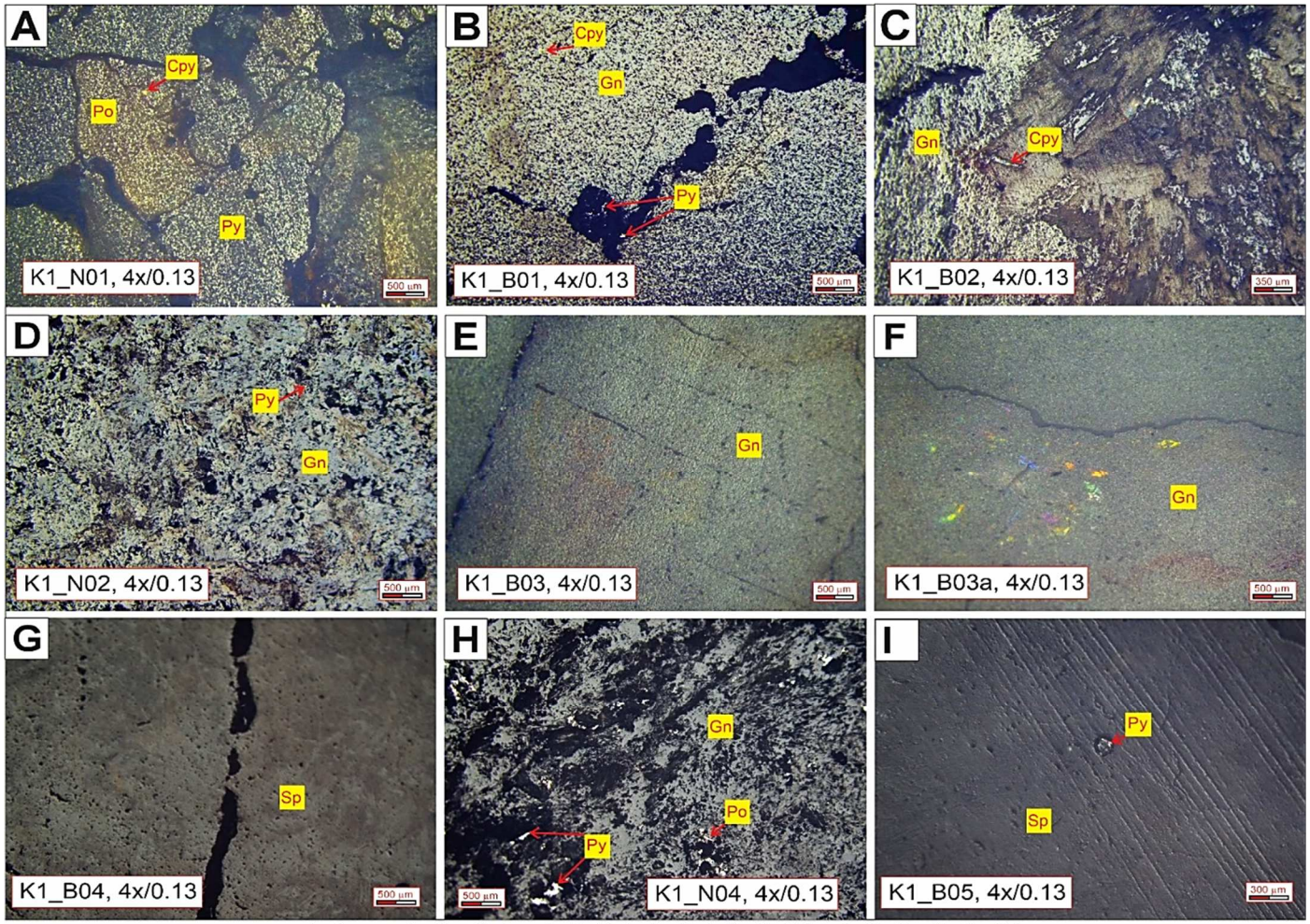

Figure 17. Photomicrographs of BQVs from the K1 prospect under reflected light: (A) Pyrrhotite and pyrite in the boudin neck with minor chalcopyrite; (B) boudin dominated by galena containing small chalcopyrite grains and gangue-filled fractures with disseminated pyrite; (C) boudin sample with galena containing small, disseminated chalcopyrite grains; (D) boudin neck sample with pyrite grains in a massive matrix of galena; (E & F) boudin sample dominated by galena; (G) boudin sample from the Spes Bona Member dominated by sphalerite with gangue-filled crack; (H) disseminated pyrite and pyrrhotite in galena; (I) pyrite grain with gangue rims in massive sphalerite.

Sulfides found in fractures provide evidence of localized remobilization, indicating that during deformation spaces were created for fluid transport and subsequent mineral precipitation, leading to the redistribution of metals (Kampmann *et al*., 2018; Rincon *et al.*, 2024). Pyrrhotite forms a rim around chalcopyrite, which signifies replacement of chalcopyrite by pyrrhotite (Figs 9B & D). Pyrrhotite is often more stable at lower temperatures and can form under reducing conditions, which may promote the breakdown of chalcopyrite and its subsequent replacement (Craig & Vokes, 1993), indicating retrograde metamorphism. Conversely, pyrite growth, recrystallization, and alteration to pyrrhotite probably occurred during prograde metamorphic conditions. The presence of fractures in sphalerite and covellite is consistent with the brittle deformation that occurs after ductile deformation has ceased. Sphalerite and chalcopyrite healing of fractures in pyrite, and the development of 'durchbewegung' textures are best explained as a consequence of dislocation flow during metamorphism and deformation under conditions comparable to regional metamorphism (e.g. Cook *et al*., 1993; Marshall & Gilligan, 1993; Zhao *et al*., 2021).

Apparent boudinage

Boudinage in intrusive sheets or dykes may result from extension and competence contrast with the host rock (Bons *et al*., 2004). Although such structures can resemble strings of lenses or beads, their intrusive nature becomes evident upon closer examination (Bons *et al*., 2004). Individual segments are irregular in shape, and layering is commonly continuous between them (Figs 14B & 15A). A foliation, which typically trends 45˚ angles to the vein, only develops when dykes intrude into hot rocks and magma solidifies slowly enough to allow the development of beads (Bons *et al*., 2004). Monoclinic symmetry is usually present in the deflection of the main foliation, particularly where bead strings and foliation (S_1) form a relatively small angle (Bons *et al*., 2004). The maximum elongation of the short and flattened, rod-shaped beads ranges from vertical to 45˚ (Fig. 17A; Bons & Druguet, 2007). They occasionally display partially split geometries that resemble pinch and swell structures.

Quartz veins in shear zones within the marble - dolomitic marble unit (MDM) at the K1 prospect exhibit features consistent with a high-strain boudinage model (Bons *et al*., 2004; Fig. 18). The K1 prospect preserves clear evidence of magmatic activity, including dyke-like intrusions of minor mafic magma and abundant pegmatites. As illustrated in figure 18C, the boudinage model is characterized by zones of elevated strain between boudins, in contrast to the inflation model (Fig. 18B; Bons *et al*., 2004), where maximum strain occurs at the corners of expanding beads and decreases away from them. In the inflation model, beads form from an intruding pegmatite dyke that disintegrates into bead-like segments through localized collapse and inflation, without stretching parallel to the bead string; typically, they terminate in narrow, crack-like tips. Such intrusions are thought to occur under peak metamorphic conditions, when the host rock approaches anatexis and is capable of ductile flow around the beads (Bons *et al*., 2004). These conditions are consistent with observations made in the study area, where deflated quartz veins are preferentially developed within shear zones of the MDM unit of the Okawayo Member (Figs 13, 14 & 15A).

Relationship between boudinage structures and sulfide redistribution

Sulfide redistribution in BQVs occurs because of deformation during the boudinage of quartz veins. The formation of boudins is controlled by the rheology of the material under deformation and results in the mechanical remobilization of sulfides. These boudinage structures likely created zones of differential stress and localized deformation, which facilitated the redistribution of sulfides by promoting fluid flow and mineral remobilization along fractures, boudin necks, and pressure shadows. Ductile sulfides, such as chalcopyrite and pyrrhotite, accommodate deformation mainly through plastic flow, whereas more brittle sulfides, like pyrite, are prone to fracturing under stress. This results in a massive matrix of ductile sulfides in the boudin necks. Temperature exerts a strong control on sulfide mineral stability and redistribution through phase transformations, recrystallization, and redox-coupled dissolution–reprecipitation reactions (Qian *et al*., 2011; Zhang *et al*., 2020). This is also true in boudinaged quartz veins since temperature changes occur during deformation. Sulfides are stable at specific temperature conditions, i.e. pyrite is stable over a broad temperature range, while pyrrhotite is favored at higher tempera-

tures under reducing conditions, and chalcopyrite commonly forms at moderate to high temperatures, often replacing earlier iron sulfides (Barton & Toulmin, 1966; Lusk & Maxwell Bray, 2002; Qian *et al*., 2011; Zhang *et al*., 2020; Frenzel *et al*., 2022). Accordingly, the replacement of sulfides by other sulfides occurs at different temperatures (Craig & Vokes, 1993).

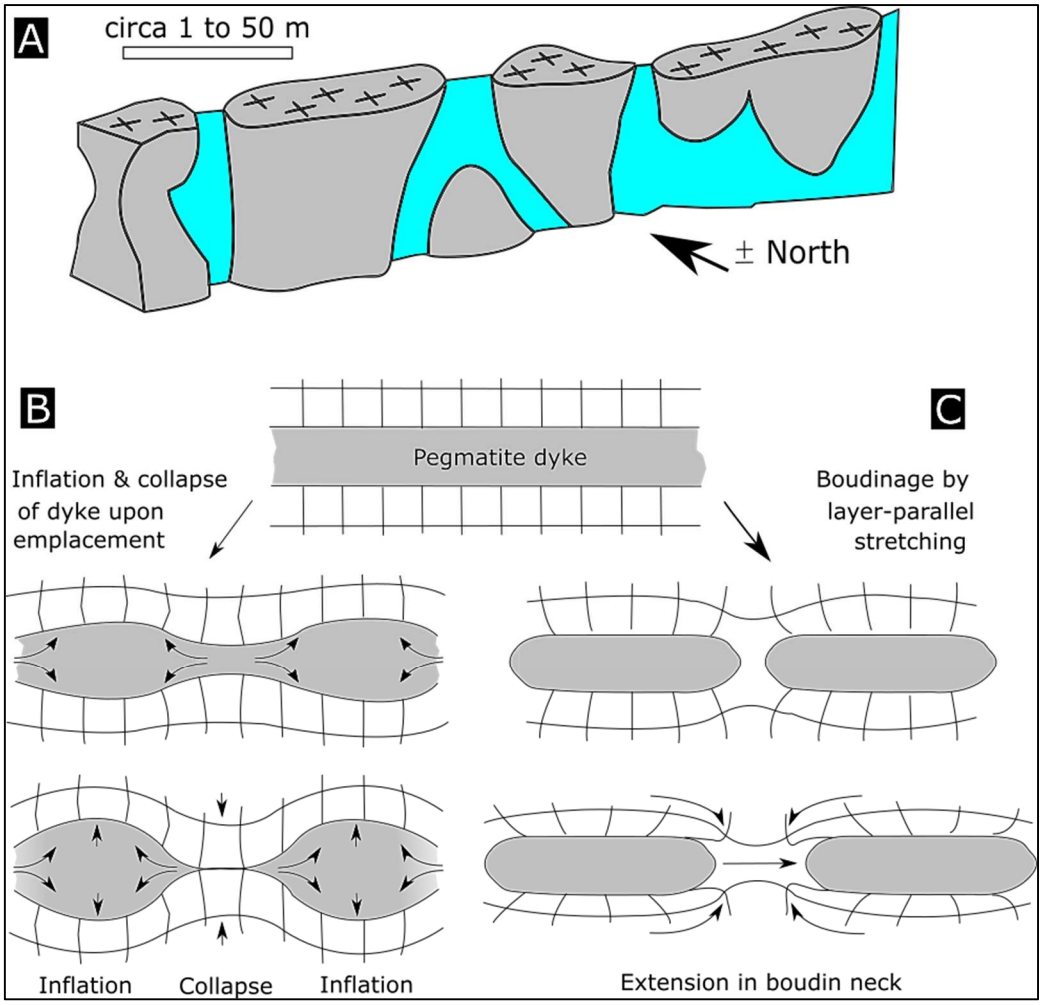

Figure 18. (A) Schematic drawing of the three-dimensional geometry of a bead string adapted from Bons *et al*. (2004): individual beads are generally elongated in the vertical direction; (B & C) schematic illustration of the two models that may lead to boudin/bead string geometries: (B) collapse and inflation of a pegmatite dyke upon emplacement, without dyke-parallel stretching; (C) boudinage of a solidified pegmatite dyke, due to dyke-parallel stretching (adapted from Bons *et al*., 2004).

Boudins

Boudins experience more strain, which causes gashes or fractures that are filled with sulfides (Williams & Blenkinsop, 2024). The most dominant sulfide minerals within boudins are chalcopyrite and pyrite containing minor arsenopyrite inclusions. Both chalcopyrite and pyrite are being replaced by pyrrhotite (Figs 9B, C, D & 12C, D). Chalcopyrite is being replaced by pyrrhotite during retrograde metamorphism. Galena occurs as a massive matrix with pyrrhotite and disseminated chalcopyrite (Fig. 9I); it may behave brittle under mechanical stress, which leads to fracturing rather than ductile deformation (Cox, 1987; Rutter, 1993; Marshall & Gilligan, 1987). Pressure applied during compaction can influence the densification of galena, which in turn affects its structural integrity and hardness (e.g. Al-Saqarat *et al*., 2024). Galena is the dominant sulfide in the marble-hosted quartz veins at the K1 prospect, whereas sphalerite is more characteristic in siliciclastic-

hosted veins. Additionally, pyrite commonly occurs intergrown with gangue minerals, typically quartz, within the massive sphalerite matrix, suggesting a complex mineralogical association influenced by local geochemical conditions.

Boudin necks

The 'durchbewegung' texture is most common in boudin necks, where competent sulfide minerals are enclosed within an incompetent sulfide matrix during remobilization (Zhao *et al*., 2021). Pyrrhotite is the most common sulfide in the boudin neck, due to the replacement of chalcopyrite and pyrite (Figs 9A, B, 12C, D, G & 19). Pyrrhotite is a common interstitial phase that typically surrounds chalcopyrite grains like a rim (Fig. 9B). This implies a sequence in which pyrrhotite replaces chalcopyrite along fractures or grain boundaries, producing a unique textural connection (e.g. Shenon, 1932.; Bischoff *et al*., 2011). Chalcopyrite can also be found as inclusions in pyrrhotite, suggesting that it either originated later because of alteration or was incorporated during the crystallization of pyrrhotite. Under certain circumstances, such as variations in temperature or pressure, the stability of chalcopyrite exceeds that of pyrrhotite, which explains why the occurrence of chalcopyrite inclusions is frequently linked to the alteration of pyrrhotite (Bischoff *et al*., 2011). Pyrrhotite undergoes partial recrystallization during deformation, resulting in the formation of coarse grains (Craig & Vokes, 1993). Covellite and sphalerite are mostly found in the boudin necks of the veins, where they occur as a massive matrix, hosting inclusions of pyrrhotite, pyrite, and chalcopyrite (Figs 7, 9 and 12). In the context of this study, sphalerite, by buffering sulphur activity, may have influenced the recrystallization process, altered stability, and modified transformation pathways during metamorphic events. This likely scenario, as described by Craig & Vokes (1993), contributes to the formation of the diverse textures observed in the sulfide minerals of boudin necks.

Implications of sulfide mobilization for gold mineralization patterns

During regional metamorphism, the shape of the orebody, spatial distribution, mineral assemblage, and ore fabric are modified.(Cook *et al*., 1993; Marshall & Gilligan, 1987). Solid state or mechanical remobilization of sulfides mostly takes place via diffusion mass transfer, continuous flow, and plastic flow (Cook *et al*., 1993; Li *et al*., 2022). In the case of the Navachab gold deposit, the replacement of chalcopyrite and pyrite by pyrrhotite, along with well-developed 'durchbewegung' textures in the boudin necks, strongly indicate sulfide remobilization. Unlike most other sulfides, which can migrate during ductile deformation, pyrite typically behaves in a more competent manner (Marshall & Gilligan, 1987; Zhao *et al*., 2021). The presence of pyrite inclusions within pyrrhotite provides evidence of 'durchbewegung'. The most common manifestation of this texture is the ocurrence of small gangue minerals, usually quartz, included in pyrrhotite, which is primarily observed in the boudin necks of boudinaged quartz veins.

Gold is liberated from earlier auriferous pyrite through processes strongly indicative of coupled dissolution–reprecipitation (CDR), which result in the presence of native gold and accessory sulfide phases, and gold can be preserved within pyrite (Hastie *et al*., 2020). According to this study, decoupling of gold and silver during remobilization resulted in the Au/Ag ratio in early pyrite changing from 0.5 - 5 to around 9 in the new native gold (900 Au purity), and incorporation of Ag into cogenetic secondary mineral phases (such as chalcopyrite, tetrahedrite, and galena). At the Navachab Gold Mine, chalcopyrite and galena are commonly found within the boudins of quartz veins, where relatively low gold grades are observed. In contrast, the boudin necks of the veins, which are dominated by pyrrhotite, pyrite, covellite, and sphalerite, are associated with higher gold concentrations (Figs 8 & 11).

Comparative analysis of mineralization between K1 prospect and Navachab main pit

One of the hypotheses of this study was that the remobilization processes and mineralogy in the two study areas, i.e. K1 prospect and Navachab main pit (Fig. 2), are relatively similar. This hypothesis was supported by previous literature (e.g. Johnson, 2005; Kisters *et al*., 2004), which highlighted similarities in geological setting, stratigraphy, and deformation events. However, the results show that despite all these resemblances, remobilization differs in the two areas.

The BQVs of the main pit are far more developed in terms of remobilization and mineralization than those at the K1 prospect. Quartz

veins in the main pit show definite boudinage structures with visible sulfides (Figs 5, 6, 8, 9, 11 & 19). On the other hand, at K1 quartz veins in the siliciclastic units do not show any signs of boudinage (Fig. 14B). This relates to K1 being located in a fold hinge of the Usakos Dome, which influenced deformation mechanisms and intensity, and consequently affected sampling. The veins exhibit more intense deformation (identified as apparent boudinage) within the Okawayo marble than in the adjacent schists; this probably reflects the lower competence of the marble and its greater ability to accommodate strain under metamorphic conditions (Figs 13 & 15), which in turn affects the remobilization process. Veins at the K1 prospect are densely distributed on the limbs toward the fold hinge of the regional Z-fold of the Usakos Dome (Fig. 13), as the less competent layers display non-planar cleavage reflecting variation in the orientation of the local XY-plane, which leads to fracturing and vein formation (Fig. 15E; Robert & Stromgard, 1972).

Results from geochemical Au-assays show that samples from the Navachab main pit have higher gold concentrations, with the highest value found in the boudin neck domain (26.95 ppm; Fig. 19) and the lowest in the boudin body domain (0.03 ppm; Figs 8 & 11). In contrast, at the K1 prospect the maximum gold grade is 2.39 ppm in the neck domain, with a minimum of 0.03 ppm also in the neck domain (Fig. 15). K1 is primarily characterized by fine, widely spaced grains of pyrite, pyrrhotite, chalcopyrite, and galena. Quartz veins from marble units are dominated by pyrite, pyrrhotite, chalcopyrite, and galena, while sphalerite is more prominent in samples collected from the schist units. Samples collected from schist units at K1 show no significant remobilization textures, enhancing the differences between the two study areas (K1 prospect and Navachab main pit), which are clearly reflected in both petrographic observations and Au-assay results.

Conclusions

Thie purpose of this study was to investigate sulfide remobilization in boudinaged quartz veins (BQVs) at the Navachab Gold Mine main pit (Karibib Dome) and the nearby K1 prospect within the Usakos Dome through integration of field observations, petrographic analysis, and geochemical Au-assays. The results confirm that in the Navachab main pit, boudin necks are preferential sites of gold enrichment relative to boudin bodies (Figs 9A, B, 12C, D, G & 19), consistent with enhanced sulfide concentration and deformation-driven fluid flow during extension. Well-developed boudinage is associated with higher strain and localized fracturing, facilitating sulfide remobilization along boudin necks, fractures, and pressure shadows, whereas vein thickness does not exert a primary control on this process.

In contrast, structures at the K1 prospect previously interpreted as boudinage are demonstrated to represent apparent boudinage formed by vein or dyke inflation and subsequent collapse. These structures lack microstructural and geochemical evidence for sulfide remobilization and are associated with comparatively low Au-grades, indicating a fundamentally different formation mechanism and mineralization potential.

New key contributions of this study include:

1. the identification of covellite and galena within the Navachab main pit at a microscopic scale, not previously reported;
2. dominant pyrrhotite with minor pyrite, covellite and chalcopyrite in the neck of boudinaged quartz veins;
3. presence of chalcopyrite and sphalerite with minor pyrrhotite and pyrite in boudin fractures;
4. ‘durchbewugung‘ as microstructural evidence linking deformation intensity to sulfide remobilization;
5. veins of different thickness have approximately the same neck to boudin Au-ratio;
6. first detailed small-scale geological and petrographic assessment of the K1 prospect, establishing the presence of apparent boudinage, lack of remobilization, and limited gold potential.

These findings refine the understanding of the relationship between deformation, vein geometry, and sulfide behavior in BQVs, and highlight the importance of distinguishing between true and apparent boudinage in evaluating gold mineralization processes and exploration targets.

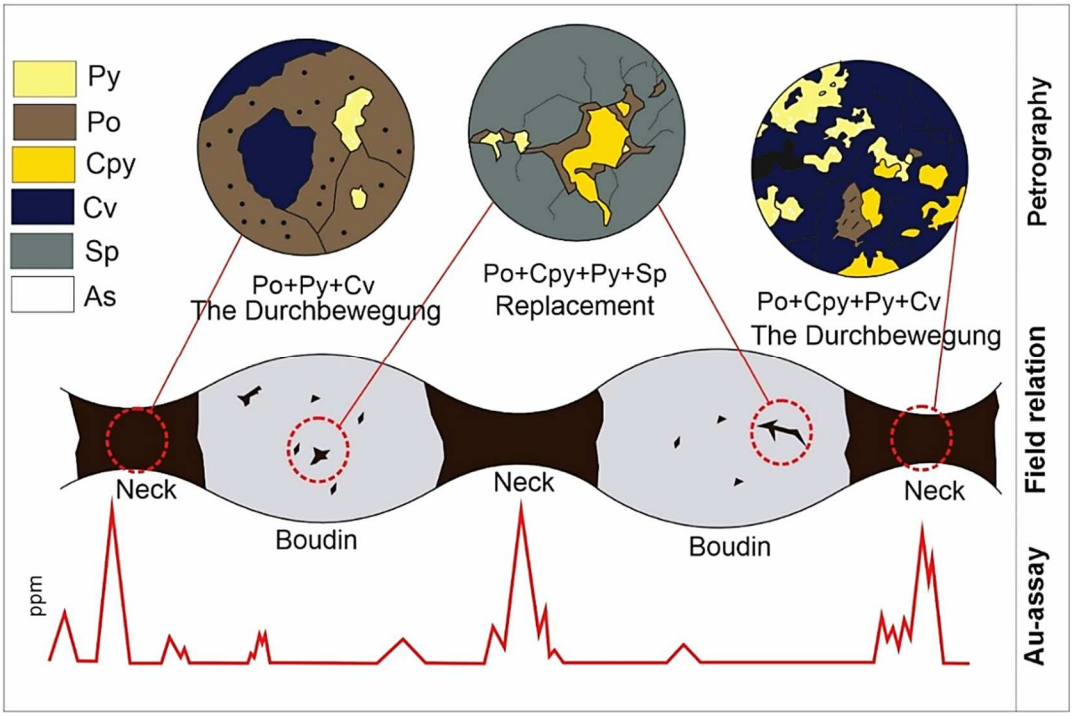

Figure 19. The diagram shows the implications of sulfide remobilization for gold mineralization, based on field relations, petrographic studies, and Au-assays. Petrography summarizes the distribution and texture of sulfides in both the boudin body and neck, with the most significant being 'durchbewegung' textures in the neck and rim replacement of chalcopyrite and pyrite by pyrrhotite. Field relations prove that sulfides appear more massive in the boudin neck than in the boudin, where they form fracture infills and disseminations. Au-assays indicate a relative pattern within the BQVs, with the neck having higher gold grades than the boudin. However, at K1 the opposite of this has been observed, which might be a result of apparent boudinage, leading to different mineralization controls or none at all.

Acknowledgments

We would like to thank the QKR Navachab Gold Mine for facilitating this study and permission to publish the results. We express our sincere gratitude for the contribution of the Navachab geology department, especially the exploration section, to field work, sampling permission, data collection and throughout the writing-up process. Special thanks go to Richard Manyanga for his unwavering support and expertise, and to the Namibian Ministry of Mines and Energy for assisting with our petrographic analysis and permission to use their microscopes at short notice. We acknowledge the insightful input of Alexander Kisters during field work. Finally, we would like to thank the University of Namibia Geology Department for arranging all necessary aspects of the study.

References

Aghaei, M., Rastad, E., Shamanian, G.H. & Madanipour, S. 2023. Characteristics of the gold-bearing and barren quartz veins at the Zaylik-Sarilar epithermal deposit, Ahar-Arasbaran Zone, NW Iran: Evidence from mineralogy, alteration, texture and fluid inclusion. *Ore Geology Reviews*, **154**, https://doi.org/10.1016/j.oregeorev.2023.105341

Al-Saqarat, B.S., Al-Mobydeen, A., Al-Dalahmeh, Y., Al-Masri, A.N., Altwaiq, A., Hamadneh, I., Abu-Afifeh, Q., Zoubi, M.M., Esaifan, M., Moosa, I.S. & Al Shamaileh, E. 2024. Study of Galena Ore Powder Sintering and Its Microstructure. *Metals*, **14(4)**, https://doi.org/10.3390/met14040439

Altman, D.G. & Bland, J.M. 1983. Measurement in medicine: the analysis of method

comparison studies. *The Statistician*, **32(3)**, 307-317.

Amponsah, P. O., Salvi, S., Béziat, D., Siebenaller, L., Baratoux, L. & Jessell, M. W. 2015. Geology and geochemistry of the shear-hosted Julie gold deposit, NW Ghana. *In*: Jessel, M. & Liégeois, J.-P. (eds), Tectonics, mineralisation and regolith evolution of the West African Craton. *Journal of African Earth Sciences (special issue)*, **112**, 505–523.

Badenhorst, F.P. 1988. The lithostratigraphy of the Chuos mixtite in part of the southern Central Zone of the Damara Orogen, South West Africa. *Communications of the Geological Survey of South-West Africa/Namibia*, **4**, 103-110.

Badenhorst, F.P. 1992. *The lithostratigraphy of area 2115 B and D in the Central Zone of the Damara Orogen, Namibia: with emphasis on facies changes and regional correlation*. M. Sc. Thesis, University of Port Elizabeth, South Africa, 124 pp.

Bamberg, B., von Hagke, C., Virgo, S. & Urai, J.L. 2022. Spacing and strain during multiphase boudinage in 3D. *Journal of Structural Geology*, **161**, https://doi.org/10.1016/j.jsg.2022.104636

Barnes, R.G. 1987. Multi-stage mobilization and remobilization of mineralization in the Broken Hill block, Australia. *Ore Geology Reviews*, **2(1)**, 247–267.

Barnes, S.J., Piña, R. & Le Vaillant, M. 2018. Textural development in sulfide-matrix ore breccias in the Aguablanca Ni-Cu deposit, Spain, revealed by X-ray fluorescence microscopy. *Ore Geology Reviews*, **95**, 849–862.

Barton, P.B. & Toulmin, P. 1966. Phase relations involving sphalerite in the Fe-Zn-S system. *Economic Geology*, **61(5)**, 815–849.

Biagioni, C., D'Orazio, M., Fulignati, P., George, L.L., Mauro, D. & Zaccarini, F. 2020. Sulfide melts in ore deposits from low-grade metamorphic settings: Insights from fluid and Tl-rich sulfosalt microinclusions from the Monte Arsiccio mine (Apuan Alps, Tuscany, Italy). *Ore Geology Reviews*, **123**, https://doi.org/ 10.1016/j.oregeorev.2020.103589

Bischoff, A., Vogel, N. & Roszjar, J. 2011. The Rumuruti chondrite group. *Geochemistry*, **71(2)**, 101–133.

Bons, P.D. & Druguet, E. 2007. Some misleading boudin-like structures. *Geogaceta*, **41**, 31-34.

Bons, P.D., Druguet, E., Hamann, I., Carreras, J. & Passchier, C.W. 2004. Apparent boudinage in dykes. *Journal of Structural Geology*, **26(4)**, 625–636.

Brandt, R. 1985. Preliminary report on the stratigraphy of the Damara Sequence and the geology and geochemistry of the Damaran granites in the area between Walvis Bay and Karibib. *Communications of the Geological Survey of South-West Africa/Namibia*, **1**, 31-43.

Cook, N.J., Halls, C. & Boyle, A.P. 1993. Deformation and metamorphism of massive sulfides at Sulitjelma, Norway. *Mineralogical Magazine*, **57(386)**, 67–81.

Cox, S.F. 1987. Flow mechanisms in sulfide minerals. *Ore Geology Reviews*, **2(1)**, 133–171.

Craig, J.R. & Vokes, F.M. 1993. The metamorphism of pyrite and pyritic ores: An overview. *Mineralogical Magazine*, **57(386)**, 3-18.

Creus, P.K. 2011. *Geology and structural controls of lode-gold mineralization around the Navachab Gold Mine in the Pan-African Damara Belt of Namibia*. M.Sc. Thesis, University of Stellenbosch, South Africa, 160 pp.

De Carvalho, A. 2019. *Controls on the diversity of the fault slip styles at the brittle-ductile transition: Examples from the Cape Fold Belt, Nuy Valley, South Africa*. M.Sc. Thesis, University of Cape Town, South Africa, 79 pp.

De Roo, J.A. & Van Staal, C.R. 2003. Sulfide Remobilization and Sulfide Breccias in the Heath Steele and Brunswick Deposits, Bathurst Mining Camp, New Brunswick. *In*: Goodfellow, W. D., McCutcheon, S.R. & Peter, J.M. (eds), Massive Sulfide Deposits of the Bathurst Mining Camp, New Brunswick, and Northern Maine. *Economic Geology Monograph Series*, **11**. Society of Economic Geologists, Littleton, Colorado, USA.

Dziggel, A., Wulff, K., Kolb, J. & Meyer, F.M. 2009. Processes of high-T fluid–rock interaction during gold mineralization in carbonate-bearing metasediments: The Navachab gold deposit, Namibia. *Mineralium Deposita*, **44(6)**, 665–687.

Frenzel, M., Voudouris, P., Cook, N.J., Ciobanu, C.L., Gilbert, S. & Wade, B.P. 2022. Evolution of a hydrothermal ore-forming system recorded by sulfide mineral chemis-

try: A case study from the Plaka Pb–Zn–Ag Deposit, Lavrion, Greece. *Mineralium Deposita*, **57(3)**, 417–438.

Gaboury, D. 2019. Parameters for the formation of orogenic gold deposits. *Applied Earth Science*, **128(3)**, 124–133.

Goldfarb, R.J. & Groves, D.I. 2015. Orogenic gold: Common or evolving fluid and metal sources through time. *Lithos*, **233**, 2–26.

Goldfarb, R.J., Groves, D.I. & Gardoll, S. 2001. Orogenic gold and geologic time: A global synthesis. *Ore Geology Reviews*, **18(1)**, 1–75.

Goldfarb, R.J., Baker, T., Dubé, B., Groves, D.I., Hart, C.J.R. & Gosselin, P. 2005. Distribution, Character, and Genesis of Gold Deposits in Metamorphic Terran, 405-450. *In*: Heden-quist, J.W., Thompson, J.F.H., Goldfarb, R.J. & Richards, J.P. (eds), *One Hundredth Anni-versary Volume*, Society of Economic Geo-logists, Littleton, Colorado, USA.

Goldfarb, R., Qiu, K., Deng, J., Chen, Y. & Yang, L. 2019. Chapter 8: Orogenic Gold Deposits of China. *In*: Chang, Z. & Goldfarb, R. J. (eds), Mineral Deposits of China, *Special Publications of the Society of Economic Geologists*, **11**.

Goscombe, B.D., Passchier, C.W. & Hand, M. 2004. Boudinage classification: End-member boudin types and modified boudin structures. *Journal of Structural Geology*, **26(4)**, 739-763.

Goscombe, B., Foster, D.A., Gray, D. & Wade, B. 2017. Metamorphic response and crustal architecture in a classic collisional orogen: The Damara Belt, Namibia. *Gondwana Research*, **52**, 80–124.

Gray, D.R., Foster, D.A., Meert, J.G., Goscombe, B.D., Armstrong, R., Trouw, R.A.J. & Passchier, C.W. 2008. A Damara orogen perspective on the assembly of southwestern Gondwana, 257-278. *In*: Pankhurst, R.J., Trouw, R.A.J., De Brito Neves, B.B. & De Wit, M. J. (eds), West Gondwana: Pre-Cenozoic Correlations Across the South Atlantic Region. *Geological Society, London, Special Publications*, **294**.

Groves, D.I., Goldfarb, R.J., Gebre-Mariam, M., Hagemann, S.G. & Robert, F. 1998. Orogenic gold deposits: A proposed classification in the context of their crustal distribution and relationship to other gold deposit types. *Ore Geology Reviews*, **13(1)**, 7–27.

Hastie, E.C.G., Kontak, D.J. & Lafrance, B. 2020. Gold Remobilization: Insights from Gold Deposits in the Archean Swayze Greenstone Belt, Abitibi Subprovince, Canada. *Economic Geology*, **115(2)**, 241–277.

Helpa, V. 2015. *Interplay between mineral reaction and deformation via structural defects*. Ph.D. thesis, Universität Potsdam, Germany.

Houghton, J.L., Shanks, W.C. & Seyfried, W.E. 2004. Massive sulfide deposition and trace element remobilization in the Middle Valley sediment-hosted hydrothermal system, northern Juan de Fuca Rdge[1]. *Geochimica et Cosmochimica Acta*, **68(13)**, 2863-2873.

Jacob, R.E., Kröner, A. & Burger, A.J. 1978. Areal extent and first U-Pb age of the Pre-Damaran Abbabis Complex in the central Damara belt of South West Africa (Namibia). *Geologische Rundschau*, **67(2)**, 706-718.

Johnson, S.D. 2005. *Structural Geology of the Usakos Dome in the Damara Belt, Namibia*. M. Sc. Thesis, University of Stellenbosch, South Africa, 165 pp.

Kampmann, T.C., Jansson, N.F., Stephens, M.B., Olin, P.H., Gilbert, S. & Wanhainen, C. 2018. Syn-tectonic sulfide remobilization and trace element redistribution at the Falun pyritic Zn-Pb-Cu-(Au-Ag) sulfide deposit, Bergslagen, Sweden. *Ore Geology Reviews*, **96**, 48–71.

Kerrich, R., Goldfarb, R., Groves, D., Garwin, S. & Jia, Y. 2000. The characteristics, origins, and geodynamic settings of supergiant gold metallogenic provinces. *Science in China Series D: Earth Sciences*, **43(1)**, 1–68.

Kisters, A.F.M. 2005. Controls of gold-quartz vein formation during regional folding in amphibolite-facies, marble-dominated metasediments of the Navachab Gold Mine in the Pan-African Damara Belt, Namibia. *South African Journal of Geology*, **108(3)**, 365-380.

Kisters, A.F.M., Jordaan, L.S. & Neumaier, K. 2004. Thrust-related dome structures in the Karibib district and the origin of orthogonal fabric domains in the south Central Zone of the Pan-African Damara belt, Namibia. *Precambrian Research*, **133(3)**, 283–303.

Kitt, S. 2008. *Structural controls of auriferous quartz veins in the Karibib area, Southern Central Zone of the Pan- African Damara belt, Namibia*. M. Sc. Thesis, University of

Stellenbosch, South Africa, 145 pp.

Lehtonen, M.I., Manninen, T.E.T & Schreiber, U.M. 1996. Lithostratigraphy of the area between the Swakop, Khan and lower Omaruru Rivers, Namib Desert. *Communications of the Geological Survey of Namibia*, **11**, 65-76.

Li, L.-H., Fan, H.-R., Qui, Z.-J., Yang, K.-F., Han, J. & Zhao, G. 2022. Sulfide texture and geochemistry of the Neoarchean Hongtoushan Cu-Zn deposit (NE China): Implication for mixed-state metamorphic remobilization. *Ore Geology Reviews*, **145**, https://doi.org/10.1016/j.oregeorev.2022.104885

Li, J., Yang, Z., Song, M., Dong, L., Li, S., Wang, R., Liu, X., Li, Z., Song, Y. & Lai, C. 2023. Gold remobilization of the Sanshandao gold deposit, Jiaodong Peninsula, Eastern China: Perspective from in-situ sulfide trace elements and sulfur isotopes. *Ore Geology Reviews*, **158**, https://doi.org/10.1016/j.oregeorev.2023.105505

Longridge, L., Gibson, R.L., Kinnaird, J.A. & Armstrong, R.A. 2011. Constraining the timing of deformation in the southwestern Central Zone of the Damara Belt, Namibia, 107-135. *In*: Van Hinsbergen, D.J.J., Buiter, S.J.H., Torsvik, T.H., Gaina, C. & Webb, S.J. (eds), The Formation and Evolution of Africa: A Synopsis of 3.8 Ga of Earth History. *Geological Society, London, Special Publications*, **357**.

Lusk, J. & Maxwell Bray, D. 2002. Phase relations and the electrochemical determination of sulfur fugacity for selected reactions in the Cu–Fe–S and Fe–S systems at 1 bar and temperatures between 185 and 460 °C. *Chemical Geology*, **192(3)**, 227–248.

Marshall, B. & Gilligan, L.B. 1987. An introduction to remobilization: Information from ore-body geometry and experimental considerations. *Ore Geology Reviews*, **2(1)**, 87–131.

Marshall, B. & Gilligan, L.B. 1993. Remobilization, syn-tectonic processes and massive sulfide deposits. *Ore Geology Reviews*, **8(1-2)**, 39-64.

Marshall, B. & Mancini, F. 1994. Major- and minor-element mobilization, with implications for Ni-Cu-Fe-sulfide remobilization, during retrograde metasomatism at the Vammala Mine, southwest Finland. *Chemical Geology*, **116(3-4)**, 203-227.

Miller, R.McG. 1983. A Possible Model for the Damara Orogen in the Light of Recent Data, 31-34. *In*: Rast, N. & Delany, F.M. (eds), Profile of Orogenic Belts. *Geodynamics Series*, **10** American Geophysical Union (AGU).

Miller, R.McG. 2008. Neoproterozoic and Early Palaeozoic Rocks of the Damara Orogen. *In*: Miller, R.McG. (ed.). *The Geology of Namibia*, Vol. **2**, chapter 13, 410 pp. Geological Society of Namibia, Windhoek.

Miller, R.McG. 2013. Comparative Stratigraphic and Geochronological Evolution of the Northern Damara Supergroup in Namibia and the Katanga Supergroup in the Lufilian Arc of Central Africa. *Geoscience Canada*, **40(2)**, 118–140.

Owen, G.J. 2011. *Geology of the Kranzberg syncline and emplacement controls of the Usakos pegmatite field, Damara belt, Central Namibia*. M. Sc. Thesis, University of Stellenbosch, South Africa, 175 pp.

Plimer, I.R. 1987. Remobilization in high-grade metamorphic environments. *Ore Geology Reviews*, **2(1)**, 231–245.

Poli, L.C. & Oliver, G.J.H. 2001. Constrictional deformation in the Central Zone of the Damara Orogen, Namibia. *Journal of African Earth Sciences*, **33(2)**, 303-321.

Qian, J., Chen, H. & Meng, Y. 2011. Geological characteristics of the Sizhuang gold deposit in the region of Jiaodong, Shandong Province—A study on tectono-geochemical ore prospecting of ore deposits. *Chinese Journal of Geochemistry*, **30(4)**, 539–553.

Raisch, D., Staude, S. & Markl, G. 2025. Revisiting semi-massive Sulfides: Textures of sulfide-silicate interactions in magmatic sulfide deposits. *Ore Geology Reviews*, **178**, https://doi.org/10.1016/j.oregeorev.2025.106457

Rincon, J., Jansson, N., Thomas, H., Kaiser, M.C., Persson, M. F., Nordfeldt, E. & Wanhainen, C. 2024. Ore Remobilization History of the Metamorphosed Rävliden North Volcanogenic Massive Sulfide Deposit, Skellefte District, Sweden. *Economic Geology*, **119(4)**, 907–934.

Robert, D. & Stromgard, K. 1972. A comparison of natural and experimental strain patterns around hinge zones. *Tectonophysics*, **14**, 105–120.

Rodrigues, B.C. & Pamplona, J. 2018. Boudinage and shear-band boudins: A meso to micro-scale tool in structural analysis. *Journal of Structural Geology*, **114**, 280–287.

Rutter, E.H. 1993. Experimental rock deformation: Techniques, results and applications

to tectonics. *Geology Today*, **9(2)**, 61–65.

Schmitt, R.S., Fragoso, R.A. & Collins, A.S. 2018. Suturing Gondwana in the Cambrian: The Orogenic Events of the Final Amalgamation, 411-432. *In*: Siegesmund, S., Basei, M., Oyhantçabal, P. & Oriolo, S. (eds), *Geology of Southwest Gondwana*. Regional Geology Reviews. Springer, Cham, Switzerland.

Shenon, P. 1932. Chalcopyrite and pyrrhotite inclusions in sphalerite. *American Mineralogist*, **17(11)**, 514–518.

Steven, N., Creaser, R., Wulff, K., Kisters, A.F.M., Eglington, B. & Miller, J. 2014. Implications of high-precision Re-Os molybdenite dating of the Navachab orogenic gold deposit, Namibia. *Geochemistry: Exploration, Environment, Analysis*, **15(2-3)**, 125–130.

Tagirov, B. R., Trigub, A. L., Kvashnina, K. O., Shiryaev, A. A., Chareev, D. A., Nickolsky, M. S., Abramova, V. D., & Kovalchuk, E. V. 2016. Covellite CuS as a matrix for "invisible" gold: X-ray spectroscopic study of the chemical state of Cu and Au in synthetic minerals. *Geochimica et Cosmochimica Acta*, **191**, 58–69.

Van Zijl, J.S.V. & De Beer, J.H. 1983. Electrical structure of the Damara Orogen and its tectonic significance, 369-379. *In*: Miller, R. McG. (ed.), Evolution of the Damara Orogen of South West Africa/ Namibia. *Special Publications of the Geological Society of South Africa*, **11**, 515 pp.

Vokes, F.M. 1969. A review of the metamorphism of sulfide deposits. *Earth-Science Reviews*, **5(2)**, 99–143.

Vollgger, S.A., Cruden, A.R., Ailleres, L. & Cowan, E.J. 2015. Regional dome evolution and its control on ore-grade distribution: Insights from 3D implicit modelling of the Navachab gold deposit, Namibia. *Ore Geology Reviews*, **69**, 268–284.

Welch, B.L. 1947. The generalization of "Student's problem when several different population variances are involved". *Biometrika*, **34(1-2)**, 28-35.

Williams, B.J. & Blenkinsop, T.G. 2024. Strain in sulfide filled foliation boudinage structures at the Mount Isa Cu deposit, Australia. *Journal of Structural Geology*, **179**, https://doi.org/ 10.1016/j.jsg.2023.105034

Wulff, K., Dziggel, A., Kolb, J., Vennemann, T., Böttcher, M.E. & Meyer, F.M. 2010. Origin of Mineralizing Fluids of the Sediment-Hosted Navachab Gold Mine, Namibia: Constraints from Stable (O, H, C, S) Isotopes. *Economic Geology*, **105(2)**, 285–302.

Wulff, K., Steven, N.M., Hein, K.A.A. & Kinnaird, J.A. 2017. The Relationship between the Structural Orientation and the Gold Mineralisation of Quartz-Sulfide Veins in the Navachab Gold Deposit, Namibia. *Ore Geology Reviews*, **80**, 504–521.

Xu, G. & Zhou, J. 2001. The Xinqiao Cu–S–Fe–Au deposit in the Tongling mineral district, China: Synorogenic remobilization of a stratiform sulfide deposit. *Ore Geology Reviews*, **18(1–2)**, 77-94

Zhang, Y., Cai, Y., Qu, Y., Wang, Q., Gu, L. & Li, G. 2020. Two-stage fluid pathways generated by volume expansion reactions: Insights from the replacement of pyrite by chalcopyrite. *Scientific Reports*, **10(1)**, https://doi.org/ 10.1038/s41598-020-76813-9

Zhao, Z., Wei, J., Liang, S. & Gao, T. 2021. Sulfide remobilization and trace element redistribution during metamorphism and deformation at the Xitieshan Pb-Zn deposit, NW China. *Ore Geology Reviews*, **136**, https://doi.org/10.1016/j.oregeorev.2021.104170